Joule

CellPress
OPEN ACCESS

Article

Tin perovskite solar cells with >1,300 h of operational stability in N_2 through a synergistic chemical engineering approach

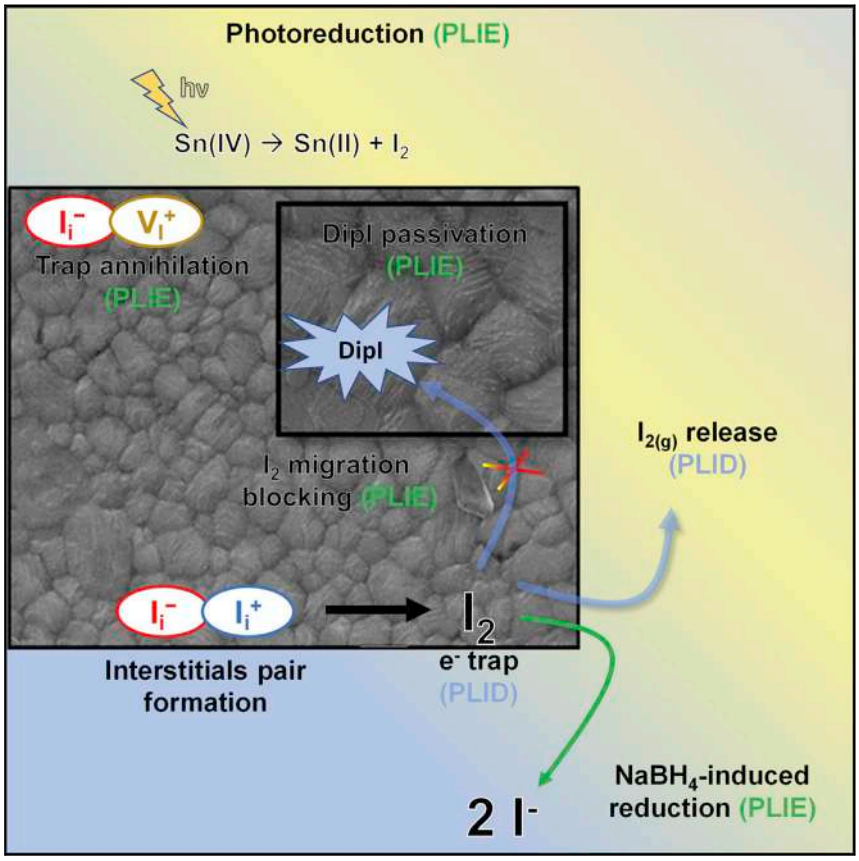

Tin-based halide perovskites are promising candidates for the development of highly efficient and low-cost photovoltaics based on low-toxicity materials. Yet, the performance of Sn-HPs solar cells is far below that of other technologies. This work focuses on enhancing the photoconversion efficiencies and extending the operational lifetime of the devices through the beneficial synergy provided by the incorporated additives. Furthermore, crucial mechanistic details that determine the performance of the devices are provided with the aim of bringing this technology one step forward.

Jesús Sanchez-Diaz, Rafael S. Sánchez, Sofia Masi, ..., Juan F. Sánchez-Royo, Juan P. Martinez-Pastor, Iván Mora-Seró

rasanche@uji.es (R.S.S.)
sero@uji.es (I.M.-S.)

Highlights

Highly efficient and long-lasting unencapsulated Sn-perovskite (Sn-HPs) solar cells

Synergistic chemical engineering approach for highly efficient and durable Sn-HPs

Elucidation of the photo-electrochemical mechanisms involved in Sn-HPs solar cells

Relevance of halide photochemistry in the performance of Sn-HPs solar cells

Sanchez-Diaz et al., Joule 6, 1–23
April 20, 2022
https://doi.org/10.1016/j.joule.2022.02.014

Please cite this article in press as: Sanchez-Diaz et al., Tin perovskite solar cells with >1,300 h of operational stability in N_2 through a synergistic chemical engineering approach, Joule (2022), https://doi.org/10.1016/j.joule.2022.02.014

Joule

CellPress
OPEN ACCESS

Article

Tin perovskite solar cells with >1,300 h of operational stability in N_2 through a synergistic chemical engineering approach

Jesús Sanchez-Diaz,[1] Rafael S. Sánchez,[1,*] Sofia Masi,[1] Marie Krecmarová,[2] Agustín O. Alvarez,[1] Eva M. Barea,[1] Jesús Rodriguez-Romero,[3] Vladimir S. Chirvony,[2] Juan F. Sánchez-Royo,[2,4] Juan P. Martinez-Pastor,[2,4] and Iván Mora-Seró[1,5,*]

SUMMARY

Despite the promising properties of tin-based halide perovskites, one clear limitation is the fast Sn^{+2} oxidation. Consequently, the preparation of long-lasting devices remains challenging. Here, we report a chemical engineering approach, based on adding Dipropylammonium iodide (DipI) together with a well-known reducing agent, sodium borohydride ($NaBH_4$), aimed at preventing the premature degradation of Sn-HPs. This strategy allows for obtaining efficiencies (PCE) above 10% with enhanced stability. The initial PCE remained unchanged upon 5 h in air (60% RH) at maximum-power-point (MPP). Remarkably, 96% of the initial PCE was kept after 1,300 h at MPP in N_2. To the best of our knowledge, these are the highest reported values for Sn-based solar cells. Our findings demonstrate a beneficial synergistic effect when additives are incorporated, highlight the important role of iodide in the performance upon light soaking, and, ultimately, unveil the relevance of controlling the halide chemistry for future improvement of Sn-based perovskite devices.

INTRODUCTION

Lead-based halide perovskites (Pb-HPs) have shown an outstanding performance in photovoltaic applications, leading to a steep increase of the PCE values from 3.8% to 25.5% in the past decade.[1–6] However, the potential risk to health and environmental hazard of Pb are clear handicaps for their commercialization.[7–9] Therefore, other elements such as antimony (Sb),[10] bismuth (Bi),[11] copper (Cu),[12] germanium (Ge),[13] and tin (Sn)[14] are currently being explored to substitute the highly hazardous Pb, as their derivatives are less toxic.[15] Among these elements, Sn has become the most promising candidate to substitute Pb because the resulting Sn-HP derivative possesses a suitable band gap of 1.2–1.4 eV, low exciton binding energy, and high carrier mobility.[16–19] Additionally, theoretical studies predict a maximum PCE value of 32.2% for formamidinium-tin-iodide ($FASnI_3$)-based HP devices,[20] unlike the low theoretical values reported for other cations.[21,22]

In this sense, great research efforts are being devoted toward the development of highly efficient Sn-HPs solar cells, and, in fact, efficiencies above 13% have been achieved so far.[23–25] However, Sn-HPs solar cells present severe stability issues. The easy oxidation of Sn^{+2} into Sn^{+4} which leads to the increase in the number of Sn^{+2} vacancies in the Sn-HPs structure and, therefore, induces the formation of

Context & scale

Despite the unprecedented achievements that solar cells based on lead perovskites have experienced in the last decades, they still suffer from essential limitations. Toxicity has been considered a handicap since the commencement of their exploitation. The stability of halide perovskites is far from being comparable to that of silicon. In addition, the photo-electrochemistry that determines their performance, the degradation paths, and the role of the additives employed is not fully understood. Tin-based perovskites alleviate the toxicity associated with lead, and we have developed a synergetic chemical strategy to enhance the performance of devices, giving special emphasis to extending the operational stability. Remarkably, our findings point to the significance of the halides' chemistry in outlining the device's performance, as well as contribute to unveiling mechanistic details that determine the photo-electrochemical processes that rule the operating principles and degradation reactions.

Please cite this article in press as: Sanchez-Diaz et al., Tin perovskite solar cells with >1,300 h of operational stability in N_2 through a synergistic chemical engineering approach, Joule (2022), https://doi.org/10.1016/j.joule.2022.02.014

high levels of self-*p*-doping and high densities of trap states,[17,26,27] limits the long-term stability of these devices dramatically. Different approaches have been proposed in order to inhibit this oxidation, such as solvent engineering[28,29] or the use of reducing agents; for example, gallic acid (GA),[30] hypophosphorous acid (H_3PO_2),[31] tin halides (SnF_2 and $SnCl_2$),[27,32–34] Sn powder,[35] or phenylhydrazine hydrochloride (PHCl)[36] have been used as additives to prevent the Sn^{+2} oxidation and improve the crystallization of the perovskite, thus leading to a pinhole-free and more homogeneous film and, consequently, enhancing the device performance. Alternative approaches found in the literature are based on the incorporation of bulky ammonium cations into the Sn-HPs, e.g., ethylenediammonium (EDA), ethylammonium (EA), or phenylethylammonium (PEA), to form more stable 2D/3D-PS derivatives that are able to provide more efficient devices.[37–45]

In this work, we introduce for the first time in the Sn-HPs thin-films a combination of dipropylammonium iodide (DipI), a secondary ammonium salt as a bulky cation, and an effective reducing agent, sodium borohydride ($NaBH_4$), with the aim of improving the performance and stability of $FASnI_3$-based solar cells. The introduction of only DipI leads to PCE values that are up to 9.06% with a remarkable long-term and thermal stability under continuous illumination, as we showed in our previous work on Pb-HPs.[46] By contrast, the reducing properties of $NaBH_4$ play the role of preventing the oxidation of Sn^{+2} into Sn^{+4} during the solution processing, which promotes an improved film crystallization and minimizes the number of crystalline defects. Therefore, we have found that employing both additives induces a synergetic effect that leads to an efficiency of 10.61% with an outstanding stability. Interestingly, our characterization demonstrates the key role of iodide/iodine in the performance increase upon light soaking and in the long-term stability, thus revealing that the control of halide chemistry is fundamental for the long-term stability of Sn-HPs solar cells.

RESULTS AND DISCUSSION

Chemical engineering approach and device application

On the basis of our previous work on $MAPbI_3$ and DipI[46] and considering the main limitations of Sn-HPs related to oxidative degradation that are generally observed in precedent works,[47,48] we decided to explore a combination of additives to synergistically induce an enhancement not only in the efficiencies but also in the long-term stability of the devices. Figure 1 shows the morphological and structural characterizations of the pristine $FASnI_3$ and those samples that contain DipI, $NaBH_4$, and their combination. Details on film preparation and the preliminary optimization of precursors and additives concentrations (Tables S1–S4) are provided in the supplemental information. Figure 1A corresponds to the SEM image obtained for the pristine $FASnI_3$ film, which shows an inhomogeneous grain distribution with the presence of numerous pinholes and significant grain size polydispersity. This phenomenon has been extensively reported due to the fast crystallization and solvent-induced Sn^{+2} oxidation during the preparation of Sn-HPs precursors solution and film deposition.[49–51] Interestingly, a clear beneficial effect is observed on the morphological features of $FASnI_3$ films upon the incorporation of our additives. Particularly, the addition of DipI induces the formation of slightly larger crystals with more defined shapes and lower surface roughness compared with the pristine films; yet, the presence of pinholes is still detected (Figure 1B). Contrarily, when $NaBH_4$ is incorporated into the $FASnI_3$ precursor solution (Figure 1C), a very compact and pinhole-free layer is obtained. Strikingly, those films obtained in the presence of both additives (Figure 1D) revealed the beneficial effects provided by both chemical species, i.e., excellent surface coverage without the presence of pinholes, large and well-defined

[1]Institute of Advanced Materials (INAM), Universitat Jaume I, Av. Sos Baynat, s/n, 12071 Castelló, Spain

[2]UMDO, Instituto de Ciencia de los Materiales, Universidad de Valencia, c/ Catedrático J. Beltrán, 2, 46980 Paterna, Spain

[3]Facultad de Química, Universidad Nacional Autónoma de México, Coyoacán, Ciudad de México 04510, México

[4]MATINÉE: CSIC Associated Unit (ICMM-ICMUV of the University of Valencia), Universidad de Valencia, Valencia, Spain

[5]Lead contact

*Correspondence: rasanche@uji.es (R.S.S.), sero@uji.es (I.M.-S.)

https://doi.org/10.1016/j.joule.2022.02.014

Please cite this article in press as: Sanchez-Diaz et al., Tin perovskite solar cells with >1,300 h of operational stability in N_2 through a synergistic chemical engineering approach, Joule (2022), https://doi.org/10.1016/j.joule.2022.02.014

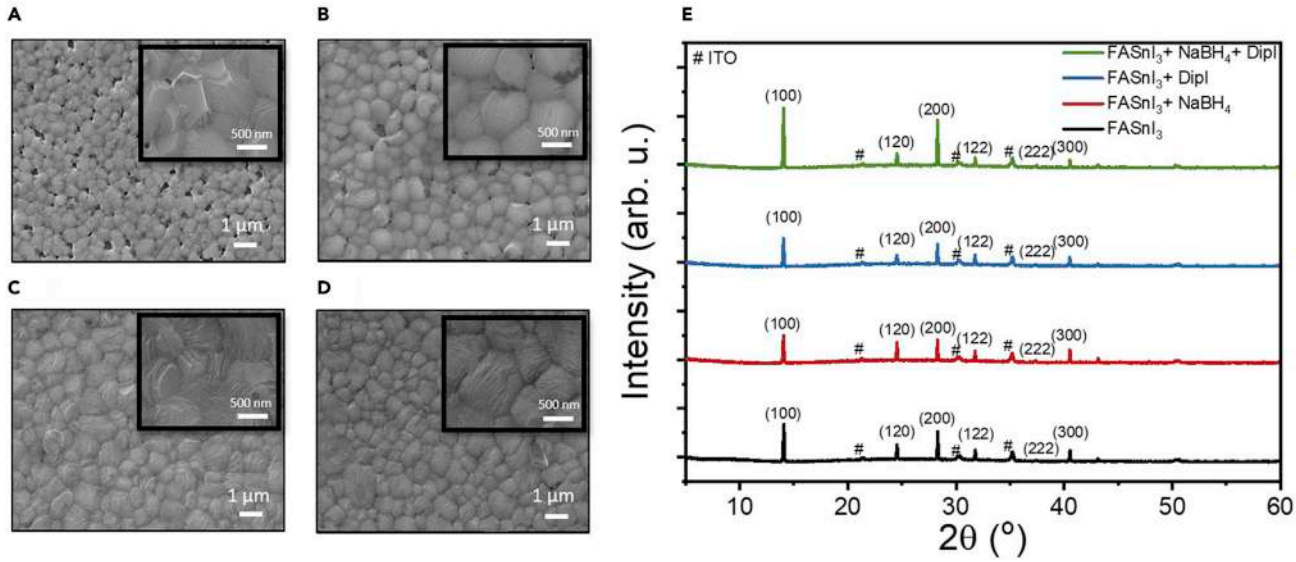

Figure 1. Morphological and structural characterization of Sn–HPS films

(A–D) Top view SEM images of (A) $FASnI_3$, (B) $FASnI_3$ + DipI, (C) $FASnI_3$ + $NaBH_4$, and (D) $FASnI_3$ + DipI + $NaBH_4$, films.

(E) XRD pattern of $FASnI_3$ films with different additives, # indicate the diffraction peaks of ITO. SEM images (A–D) were registered at the same magnification; therefore, the scale bars are equivalent.

crystalline domains, and lower surface roughness. As shown in the AFM images (Figure S1), the roughness average (Ra) was estimated to be 2.83 nm for the pristine $FASnI_3$ and 2.58 nm for the $FASnI_3$ + DipI + $NaBH_4$ films (Table S5).

Since the addition of additives seems to play a significant role on the Sn^{+2} stability (see below) and crystallization of Sn–HPS, we explored the crystallographic features of the resulting films to identify the crystal phases obtained. Figure 1E shows the XRD pattern of the $FASnI_3$ films with and without additives from which we can confirm that the same crystal phase is obtained in all cases; therefore, the addition of our additives does not affect the crystallographic properties of the Sn-HPs. In particular, six diffraction peaks were identified at 2θ angle values of 14.1°, 24.5°, 28.2°, 31.7°, 37.5°, and 40.5° ascribed to the HP matrix, which correspond to the (100), (120), (200), (122), (222), and (300) crystallographic planes, respectively, of the orthorhombic lattice (Amm2 space group).[52,53] It is worth mentioning that the analysis of the full width at half-maximum (FWHM) of the dominant peak at 14.1° (Figure S2) revealed a progressive decrease upon the addition of $NaBH_4$, DipI, and a combination of both, respectively, thus confirming the increase of crystalline domains size when the additives are incorporated.

In order to shed light onto the effect of the reducing agent on the Sn species upon light and air exposure, the absorption spectra of the HP precursor solutions with and without additives were monitored. As shown in Figure S3, all the fresh $FASnI_3$ precursor solutions (pristine $FASnI_3$, $FASnI_3$ + $NaBH_4$, $FASnI_3$ + DipI, and $FASnI_3$ + $NaBH_4$ + DipI) showed identical absorbance over the entire spectral range studied when the solutions were protected from air and light exposure. However, after light exposure at 1 sun conditions in air, significant differences were observed. Clearly, the sample without any additive showed a significant bathochromic shift of the absorption signal, which was corroborated by eye inspection of the solution that turned from being colorless to yellowish. This transformation is ascribed in precedent works to the oxidative degradation of Sn^{+2} toward the formation of SnI_4.[29,51,54,55]

Please cite this article in press as: Sanchez-Diaz et al., Tin perovskite solar cells with >1,300 h of operational stability in N_2 through a synergistic chemical engineering approach, Joule (2022), https://doi.org/10.1016/j.joule.2022.02.014

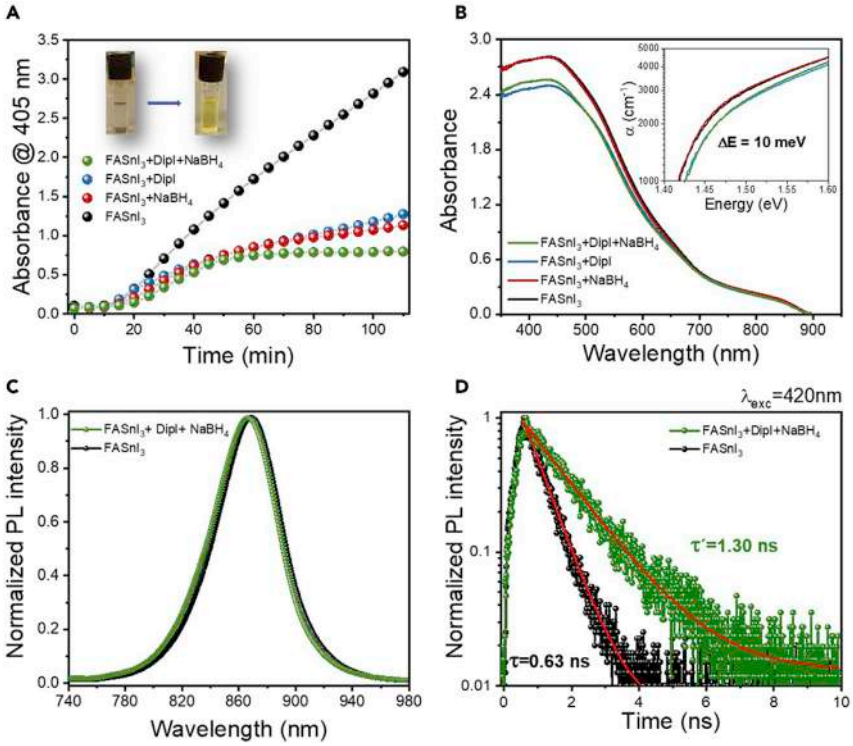

Figure 2. Optical characterization of Sn–HP precursor solutions and films

(A) Evolution of the absorbance at 405 nm of the precursor solutions with different additives upon different intervals of light exposure (1 sun) in air.

(B–D) Optical characterization of Sn-HP films deposited on glass: (B) UV-Vis spectra of $FASnI_3$ films without and with different additive formulations; inset shows the absorption coefficient, α, as function of energy in the absorption band edge region, (C) normalized PL spectra and (D) time-resolved PL decays corresponding to $FASnI_3$ without and with both additives. The first parts of the PL decays were fitted to monoexponential functions.

Interestingly, those solutions in which our additives were introduced suffered a remarkably slower evolution of the absorption signal (monitored at 405 nm), as shown in Figure 2A. In particular, the solution that contained both additives suffered lesser variations of the absorption spectrum and a faster stabilization of the absorbance at 405 nm, which confirms that the combination of both additives indeed promotes a more effective inhibition of the oxidative degradation of Sn^{+2} species compared with the samples containing a single additive composition. As a direct consequence of the oxidation prevention, which was induced by the additives incorporated into the $FASnI_3$ precursor solution, a more uniform grain size distribution and pinhole-free smooth films with reduced presence of charge-carrier traps are obtained upon HP crystallization; see Figure 2D where longer photoluminescence (PL) lifetimes are recorded for samples with additives. In order to compare the effect of incorporating DipI into the Sn-HPs precursor solution, taking phenylethylammonium iodide (PEAI) as a benchmark additive, as it is one of the most widely reported bulky cations in Sn-HPs, we explored the evolution of their absorption spectra upon exposure to light in air (Figure S4). Interestingly, the DipI solution showed a less prominent increase in the red-shifted signals compared with PEAI, thus suggesting that the alkylammonium salt used in this work may contribute to stabilize, direct or indirectly, the Sn^{+2} species more efficiently. This effect seems to be particularly crucial not only during solution preparation and handling but also along the crystallization process toward the formation of more robust semiconductors.

Please cite this article in press as: Sanchez-Diaz et al., Tin perovskite solar cells with >1,300 h of operational stability in N_2 through a synergistic chemical engineering approach, Joule (2022), https://doi.org/10.1016/j.joule.2022.02.014

Additionally, we characterized the optical properties of the $FASnI_3$ films obtained through the addition of additives and compared the results with those from the pristine Sn-HP samples. As shown in Figure 2B, the absorption spectra of $FASnI_3$ with and without additives are very similar, although a slight decrease in the absorbance is systematically observed upon the addition of DipI. Besides, the addition of DipI slightly blue-shifts the band edge absorption position, as shown in the inset of Figure 2B and Tauc plot, Figure S5, from which the band gap was determined to be 1.38 eV for both $FASnI_3$ and $FASnI_3$ + $NaBH_4$ samples and 1.39 eV for the counterpart HP films containing DipI. This small hypsochromic shift, together with the decrease in the absorbance along the UV-VIS-NIR spectral range, has been previously observed,[56,57] and it was ascribed to the insertion of the bulky cation into the HP structure. Note that samples with and without additives present similar thicknesses. The averaged thickness values were estimated to be 197 $\pm$ 40 nm and 191 $\pm$ 19 nm for $FASnI_3$ and $FASnI_3$ + DipI + $NaBH_4$, respectively, from SEM images (Figure S6).

The PL spectra of both $FASnI_3$ and $FASnI_3$ + $NaBH_4$ + DipI samples were practically identical (roughly, λ_{max} = 880 nm and FWHM = 57 nm), although, accordingly to the absorption spectra, an almost unperceivable blue-shift of 4 nm is observed for the sample containing both additives (Figure 2C). These results indicate that the use of DipI and $NaBH_4$ do not induce dramatic changes in the absorptive and emissive properties of the HP bulk, even though the bulky cation is inserted into the HP structure. However, time-resolved PL spectroscopy (TRPL) clearly revealed that the addition of DipI and $NaBH_4$ increases the charge-carrier recombination time by about 107% as compared to pristine $FASnI_3$ (Figure 2D), from τ = 0.63 ns to τ' = 1.30 ns, thus meaning that the additives lead to an efficient inhibition of the non-radiative recombination pathways.

The beneficial effect of the additives on the PL lifetime is likely due to the improvement of the Sn-HPs crystallinity and film morphology (Figure 1), since bad quality crystallization is commonly related to the presence of trap states,[40,58] in combination to an efficient inhibition of the oxidative evolution of Sn^{+2} and, therefore, lesser formation of Sn^{4+} recombination sites (see discussion below; Figure 2A).

In order to explore the suitability of our approach to improve the performance and stability of the Sn-HP solar cells, we fabricated complete devices with inverted configuration ITO/PEDOT:PSS/Sn-HP/C_{60}/BCP/Ag (active area of 0.121 cm^2), which are shown in Figure 3A along with the forward (F) and reverse (R) scans of the *J-V* curve obtained for the champion $FASnI_3$ + DipI + $NaBH_4$ device, with a PCE of 10.61%. Figure 3B shows the F-scan of the *J-V* curves obtained for the $FASnI_3$ devices that illustrate the general behavior upon the introduction of the different additive combinations. Averaged cell parameters are summarized in Table S6. The cell parameters of the representative reference device displayed in Figure 3B, i.e., pristine $FASnI_3$, shows an *open circuit voltage* (*Voc*) of 0.540 V, a *short circuit current* (*Jsc*) of 18.20 $mA \cdot cm^{-2}$, and a *fill factor* (*FF*) of 48%, which led to a low overall PCE of 4.72%.

The reduced *Voc* of Sn-based devices is systematically reported in the bibliography[59] and commonly ascribed to trap states that originated from the oxidation of Sn^{+2} to Sn^{+4}, which may act as non-radiative charge recombination centers. Non-radiative recombination in the bulk and/or at the interfaces cause the limited *Voc* in Sn-HP solar cells.[60]

Please cite this article in press as: Sanchez-Diaz et al., Tin perovskite solar cells with >1,300 h of operational stability in N_2 through a synergistic chemical engineering approach, Joule (2022), https://doi.org/10.1016/j.joule.2022.02.014

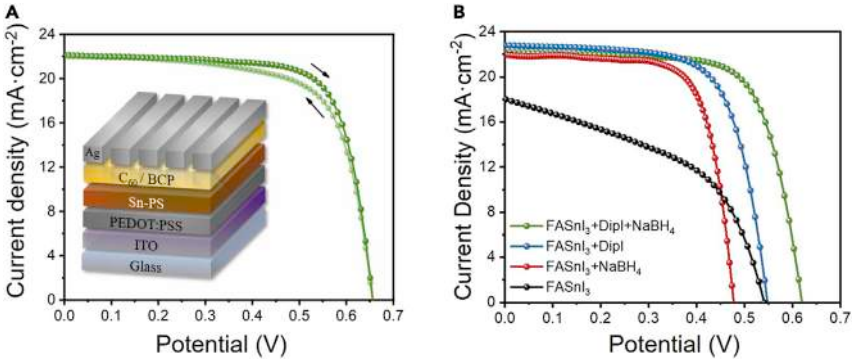

Figure 3. Photovoltaic performance

(A) F- and R-scans of the *J-V* curve for the champion $FASnI_3$ + DipI + $NaBH_4$ device; the inset shows the schematic configuration of the device.

(B) F-scan of *J-V* curves for $FASnI_3$ devices (without and with different additives) that are representative of the average behavior; see Table S6. *J-V* curves measured after 3 days of light-soaking treatment.

By contrast, *Jsc* of solar cells is mainly determined by the optical absorption of the light-active material and the efficiency of the charge extraction. For Sn-HPs with band gaps of 1.2–1.4 eV, the maximum *Jsc* could theoretically reach 40 $mA \cdot cm^{-2}$.[59] Unfortunately, the current density values reported for Sn-HP devices are far below this value due to several reasons. On one hand, the insertion of additives, e.g., reducing agents or bulky cations, into the HP layer might hamper the charge transport/extraction. On the other hand, the higher density of defects of Sn-HPs compared with Pb-HPs induces a decrease in the charge-carrier lifetime, diffusion length, and mobility and, therefore, plays a detrimental role on the charge extraction.[61] Additionally, the reported thicknesses of Sn-HP films are roughly 200–300 nm (≈200 nm in this work), which are significantly lower than the optimum value of 500 nm, according to theoretical calculations, as to ensure an optimum photon absorption.[62]

According to the literature, the FF values obtained for Sn-HP devices are also systematically lower than those obtained from the Pb-HP counterparts.[59] It has been observed that Sn-HPs undergo a fast crystallization process that promotes the formation of numerous trap states, thus favoring severe non-radiative losses and, therefore, reduced *FF*.

The results shown in Figure 3 were recorded after 3 days of continuous light soaking at 1 sun in N_2 atmosphere. The illumination treatment has a clear beneficial effect on the solar cell's performance, regardless of the presence/absence of additives (Figure S7). Therefore, unless it is specifically indicated, the provided solar cell parameters were obtained after a 3-day light soaking. The performances of the devices upon light treatment were statistically verified through the preparation of 80 devices for each composition, as presented in Figures 4A–4D and summarized in Table S6. As clearly seen, the overall results of devices for each additive composition are consistently confirmed along a significantly great number of replicas, thus allowing for the extraction of reliable conclusions. Figure S8 shows a histogram of the PCE values obtained for the Sn-based devices with and without additives, which, in turn, verifies the high reproducibility of the device's fabrication. Additionally, Table S7 and Figure S9 depict the solar cell parameters and *J-V* curves, respectively, of the champion devices for each studied composition.

Please cite this article in press as: Sanchez-Diaz et al., Tin perovskite solar cells with >1,300 h of operational stability in N_2 through a synergistic chemical engineering approach, Joule (2022), https://doi.org/10.1016/j.joule.2022.02.014

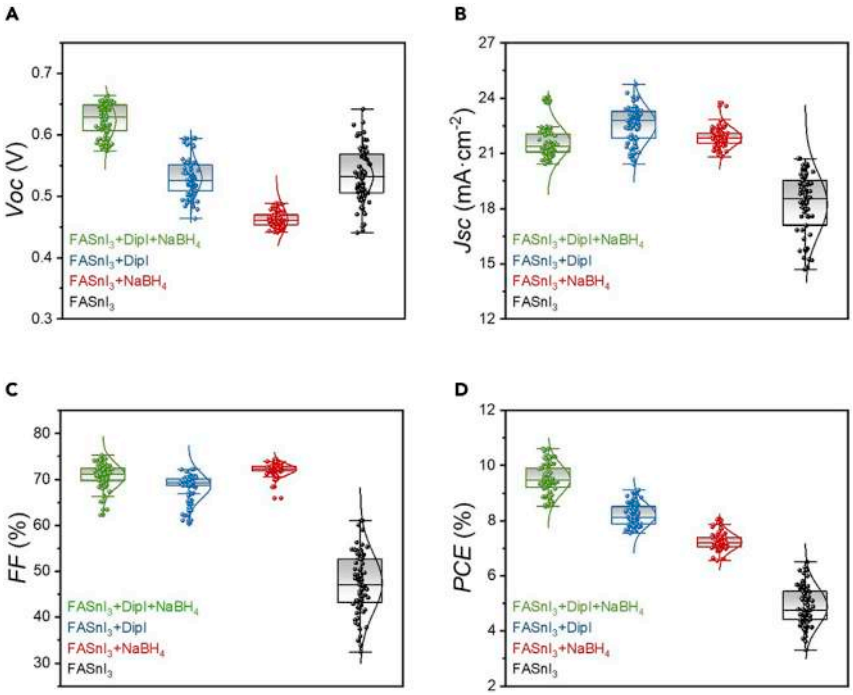

Figure 4. Statistical characterization of photovoltaic parameters

(A–D) Cell parameters obtained from the *J-V* curves based on the statistics of 80 pixels of $FASnI_3$-based devices with different additive compositions, where (A) *Voc*, (B) *Jsc*, (C) FF, and (D) PCE. The photovoltaic parameters reported here correspond to those measured after 3 days of light-soaking treatment. The median values are indicated as the horizontal lines that divide the boxes into two parts; half the scores are greater than or equal to this value and half are less. The boxes represent the middle 50% of scores for each group of values that fall within the interquartile range (IQR). The regions delimited by the upper and lower whiskers represent the scores that fall within the 1.5 IQR range.

With our chemical engineering strategy, not only the addition of solely DipI or $NaBH_4$ but also the combination of these two, interestingly, contribute to a very significant enhancement of the averaged *FF* (Figure 4C), from 47% for the pristine $FASnI_3$ devices to 69%, 72%, and 71% (Table S6). In addition, *Jsc* is also remarkably enhanced when additives are introduced (Figure 4B). Compared with the pristine $FASnI_3$, the devices containing DipI, $NaBH_4$, and DipI + $NaBH_4$ showed remarkable averaged *Jsc* values of 22.6, 21.8, and 21.8 $mA \cdot cm^{-2}$, respectively, which are much higher than the 18.20 $mA \cdot cm^{-2}$ obtained for the average reference device (Table S6). These results could be ascribed to the higher morphological quality of the films upon the addition of DipI and $NaBH_4$, as shown in SEM images (Figures 1A–1D), and the additive-induced diminishment of trap-states in the bulk and/or interfaces as supported by the increase in the PL lifetime (Figure 2D), which, in turn, enhances the charge extraction efficiency. As a result, samples with additives present higher performances than bare $FASnI_3$ samples (Figure 4D), which increased from the 4.8% obtained for the averaged reference solar cells to 7.3%, 8.3%, and 9.6% for the averaged $NaBH_4$, DipI, and DipI + $NaBH_4$ devices, respectively (Table S6). Hence, the highest performances were clearly obtained for those samples with both additives. Note that these devices also report the highest *Voc* (Figure 4A).

Although *Jsc* and FF are systematically increased when additives are added, the behavior *Voc* present differences depending on the additive used (Figure 4A).

Please cite this article in press as: Sanchez-Diaz et al., Tin perovskite solar cells with >1,300 h of operational stability in N_2 through a synergistic chemical engineering approach, Joule (2022), https://doi.org/10.1016/j.joule.2022.02.014

Whereas reference devices and $FASnI_3$ + DipI samples present similar averaged *Voc* values, 0.540 and 0.530 V, respectively, $FASnI_3$ + DipI + $NaBH_4$ presents the highest averaged *Voc* of 0.620 V. By contrast, the lowest photovoltage, 0.460 V, is obtained for $FASnI_3$ + $NaBH_4$ devices (Figure 4A; Table S6). Likewise, with the aim of fairly deconvoluting the effects induced by the additive's incorporation and light-soaking treatment, Figure S7 shows the averaged solar cell parameters, before (fresh devices) and after the 3-day light-soaking treatment, obtained from a single batch of devices prepared with the different additive combinations. As it can be observed, all the fresh devices show similar *Voc* values, whereas the rest of the cell parameters are significantly enhanced upon the incorporation of any additive combination. Note that the *Jsc*, *FF*, and PCE enhancements are especially notable for the $FASnI_3$ + DipI + $NaBH_4$ devices due to the additives-induced synergistic effect. We speculate that $NaBH_4$ introduces an additional mechanism that causes a less pronounced increase of *Voc* after light-soaking. Perhaps, the reported incorporation of BH_4^- to the perovskite structure,[63] which might inhibit other surface processes, could be behind this finding. It is very likely that the combined use of $NaBH_4$ with DipI avoids the incorporation of BH_4^- into the perovskite structure due to the passivating role of DipI; therefore, the synergistic effect that enhances the final performance of devices, with both additives incorporated, is achieved.

The forward and reverse (F- and R-, respectively) scans of the *J-V* curves obtained for the $FASnI_3$ + DipI + $NaBH_4$ champion device are shown in Figure 3A, and those corresponding to the pristine, DipI and $NaBH_4$ devices, are presented in Figure S9, with the cell parameters summarized on Table S7. Our results suggest that the addition of DipI or $NaBH_4$ leads to negligible hysteresis in comparison with the pristine $FASnI_3$ device, which shows an intense inverted hysteresis. Precedent works claim that inverted hysteresis present in some Sn-HP devices might arise from a strong non-radiative charge recombination that could be minimized upon further device optimization.[64] The pronounced hysteresis obtained for our reference devices could point to the same origin. The rough surface morphology of the HP film and the presence of pinholes would contribute to the enhancement of the interfacial charge accumulation/recombination and, therefore, determine the hysteretic behavior of the solar cells and the reduced *FF*.[65,66] Despite the fact that the *J-V* curves of our optimized $FASnI_3$ + DipI + $NaBH_4$ reveals perceivable differences between the F- and R-scans (Figure 3A), the hysteresis is indeed much lower than that obtained for the reference devices (Figure S9).

Long-term stability and light-soaking effect

Given that the beneficial role of the additives, i.e., DipI and $NaBH_4$, was unambiguously demonstrated in this work, we decided to explore their effect on the long-term film's and device's stabilities, which are the most limiting issues to be tackled nowadays in the HP-based technology field, especially for Sn-HPs. In a preliminary experiment, the absorption spectra of the freshly made films with the four different additives compositions were registered and compared with those registered upon 3 months of being stored in dark conditions in dry nitrogen. Even though the four samples retained a dark color perceivable to naked eye and displayed the characteristic XRD peaks (Figure S10), the absorption spectra of the pristine $FASnI_3$ and $FASnI_3$ + DipI films varied drastically throughout the storage period, as shown in Figure S11. By contrast, the UV-vis spectra of the $FASnI_3$ + $NaBH_4$ and $FASnI_3$ + $NaBH_4$ + DipI samples revealed comparable intensities and the characteristic absorption bands similar to those in the corresponding fresh samples. This simple experiment allowed us to verify that $NaBH_4$ is actively involved in the long-term stability of the films stored in inert conditions. The clear beneficial role toward the

stabilization of the Sn-HP films in inert atmosphere by the use of additive $NaBH_4$ is not extended to ambient atmosphere due to the high hygroscopic nature of both $NaBH_4$ and DipI, as shown in the XRD pattern in Figure S12.

Beyond film stability, the stability of solar cell devices has been systematically analyzed. To do so, we performed the stability study of a fresh unencapsulated $FASnI_3$ + DipI + $NaBH_4$ device under continuous illumination at the *maximum-power-point* (*MPP*) (100 $mW \cdot cm^{-2}$ AM1.5G at a constant voltage of 0.45 V) in ambient conditions (~60% RH); see Figure S13 and Table S8 for the *MPP* analysis of during the measurement time. Note that the stability of the films must not be necessarily correlated with the stability of the devices, as the additional layers deposited on top of the perovskite may play a protective role against moisture and oxygen; e.g., C_{60} has a hydrophobic character, adding a potential additional protection to the complete device. As shown in Figure 5A, 100% of the initial efficiency was maintained during the first 5 h, and then, a gradual drop started to occur reaching values of 96%, 93%, 88%, and 80% of the initial PCE after 6, 7, 8, and 9 h, respectively. Beyond 9 h, a faster performance decrease is observed, and, therefore, two well-differentiated efficiency-drop regions are detected:(1) a slow PCE decrease region that was ascribed to the loss of FF due to device heating (temperature raised to 60°C because of the lamp heat radiation), and (2) a fast PCE lessening region due to $FASnI_3$ oxidative degradation. In any case, it is clear that the loss of PCE matches well with the decrease of the current density (Figure 5A), and, therefore it is very likely that both phenomena, i.e., loss of FF due to heating and the oxidative degradation of $FASnI_3$, temporarily coexist upon 5 h at the measuring conditions.

Figure 5B shows the comparison between the PCE (extracted from *J-V* curves) of pristine $FASnI_3$ and $FASnI_3$ + DipI + $NaBH_4$ solar cells. The devices were kept in N_2 atmosphere under continuous illumination at 1 sun using a UV cut-off filter, and the *J-V* curves were measured every 2 h. In both cases, we observed an increment of the initial efficiency due to a significant increase of the *Voc* (Figure S14). Although both devices initially showed a similar *Voc* increase with the light soaking, the pristine $FASnI_3$ started to degrade within the first 70 h of operation and it lost 40% of the initial PCE after 200 h. Contrarily, the PCE of the $FASnI_3$ + DipI + $NaBH_4$ device gradually increased, reaching up to 130% of the initial PCE after 500 h of light exposure (Figure S15). The same analysis was also made for the $FASnI_3$ + DipI and $FASnI_3$ + $NaBH_4$ devices, which showed a similar effect, although at slightly different rates. The $FASnI_3$ + DipI device displayed a rapid increment of the PCE within the first 100 h and reached the maximum efficiency after 500 h (150% of the initial PCE) and then decreased slowly, but after 1,000 h, it still retained 111% of the initial efficiency. The PCE drop was mainly ascribed to the loss of FF. Interestingly, the *Voc* and *Jsc* were insignificantly modified (Figure S16). The positive effect of light-soaking in Sn-HP solar cells has been previously reported[43]; however, its origin has not been clearly identified yet.

On the basis of this phenomenon, we currently introduce the light-soaking treatment as a part of the device fabrication aimed at enhancing the *Voc* of our devices. We determined that a continuous illumination (100 $mW \cdot cm^{-2}$, AM1.5G) in N_2 atmosphere during 3 days is optimal for maximizing the solar cells performances. Figure S17 shows the resulting cell parameters before and after different days of light soaking. As mentioned before, the *Voc* is the main enhanced parameter that induces an increase in the PCE. Despite the other cell parameters not suffering dramatic variations within the first 3 days, the FF suffered a slight drop upon 5 days of light exposure, and consequently, the efficiency slightly decreased. In order to further study

Please cite this article in press as: Sanchez-Diaz et al., Tin perovskite solar cells with >1,300 h of operational stability in N_2 through a synergistic chemical engineering approach, Joule (2022), https://doi.org/10.1016/j.joule.2022.02.014

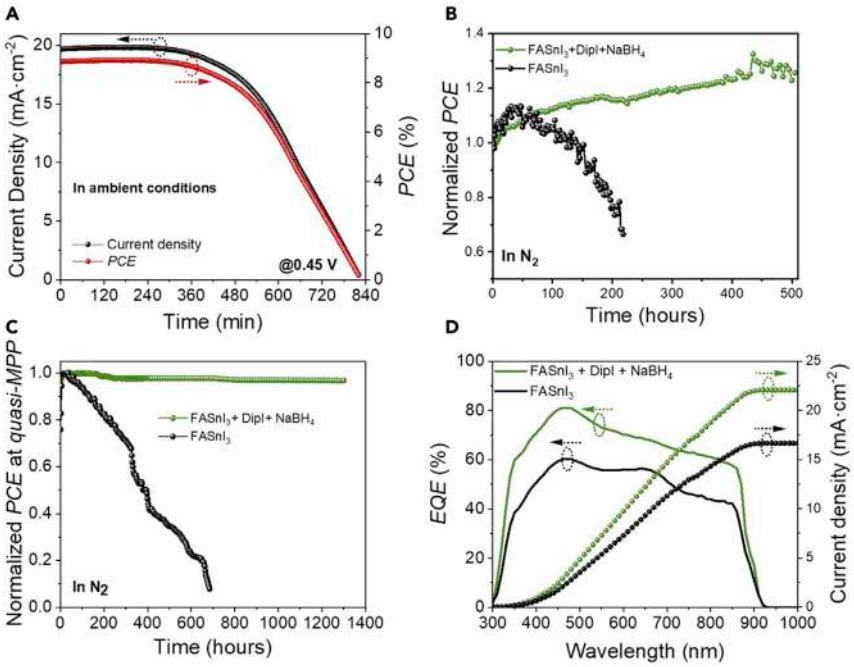

Figure 5. Stability of devices

(A) Stability test under illumination (AM1.5G, 100 mW·cm^{-2}) of the $FASnI_3$ + DipI + $NaBH_4$ device at MPP in ambient conditions (~60% RH) without encapsulation.

(B and C) Stability comparison of the unencapsulated $FASnI_3$ and $FASnI_3$ + DipI + $NaBH_4$ devices under continuous illumination: (B) normalized *PCE* extracted from *J-V* measurements under continuous illumination (1 sun) every 2 h in N_2 atmosphere and (C) normalized PCE at MPP in N_2 atmosphere.

(D) EQE spectrum and integrated current of the pristine $FASnI_3$ and $FASnI_3$ + DipI + $NaBH_4$ devices. MPP and long-term stability measurements (air or N_2) were measured under continuous illumination (calibrated Xenon lamp at 100 mW·cm^{-2}). A fixed voltage corresponding to V_{MPP} (determined for each sample from the *J-V* curves, after applying a 3-days light-soaking treatment) was applied for the MPP measurements, and the electrical photocurrent I_{MPP} was monitored over time. See supplemental information. for further details.

the stability of the $FASnI_3$ + DipI + $NaBH_4$ devices and compare it with that of the pristine $FASnI_3$ devices, we monitored the photocurrent at the *MPP* operation in N_2 atmosphere (at a constant bias of 0.3 V for pristine and 0.42 V for $FASnI_3$ + DipI + $NaBH_4$, the original V_{MPP} values of the fresh devices without light soaking). As shown in Figure 5C, the initial PCE of the pristine $FASnI_3$-based device was kept for the first 26 h. Then, a steep decrease was identified and correlated with the degradation of the light-absorber layer, i.e., HP film. Very interestingly, the $FASnI_3$ + DipI + $NaBH_4$ device kept the initial PCE after 170 h at *MPP* and then retained 96% of the initial PCE at least during 1,300 h. These experiments confirmed the outstanding stability behavior of the $FASnI_3$ + DipI + $NaBH_4$, considering that the most stable Sn-HP-based devices (encapsulated) reported up to date last for 1,000 h under continuous illumination at *MPP*, maintaining 95% of its initial PCE values (Table S9).[42,67] Therefore, we have been able to confirm that our approach based on chemical engineering provides valuable insights toward the fabrication of highly efficient and stable Pb-free HP solar cells.

Eventually, it is worth remarking the good agreement between the photocurrent measured from the *J-V* curves and that obtained from the integration of the external quantum efficiency (EQE) for the pristine $FASnI_3$ and $FASnI_3$ + DipI + $NaBH_4$ devices

Please cite this article in press as: Sanchez-Diaz et al., Tin perovskite solar cells with >1,300 h of operational stability in N_2 through a synergistic chemical engineering approach, Joule (2022), https://doi.org/10.1016/j.joule.2022.02.014

(Figure 5D). The EQE spectra show a wide photo response from the visible to the IR region, which also agrees well with the absorption spectra shown in Figure 2A. Note that the increase in photocurrent response for the sample with additives can be observed along the entire photoactive spectral range.

All these results clearly demonstrate the beneficial contribution of our additives toward the development of a highly efficient and durable Sn-HP-based photovoltaics technology; however, the mechanisms behind the performance improvement must be identified. In this sense, we have made a systematic characterization in order to clarify the origin of the performance improvement upon light soaking and identify the mechanisms behind the superior performance observed for the devices with additives.

Figure 6A shows the Sn 4d and I 3d XPS spectra of the fresh films based on both compositions, i.e., $FASnI_3$ without and with both additives. Interestingly, the films containing additives showed significantly larger Sn^{+2}/Sn^{+4} and I^-/I_2 ratios, which is in excellent agreement with the expected role of our additives as oxidation inhibitors, as the experiment shown in Figure 2A suggested, thus explaining the initial higher performance of the samples with additives. The sensitivity of the XPS technique is limited only to the first few nanometers below the surface of the films. At the surface, defects and dangling bond sites are inevitably present and their reactivity is believed to be remarkably high. Consequently, the observation of a large fraction of Sn^{+2} ions on XPS, even at the surface of the fresh samples, is already indicative of the high quality of the samples, as the Sn^{+4} content in the bulk of our films is drastically lower (see the below discussion; Figure 6C).

We have demonstrated that light soaking the Sn-based solar cells in inert atmosphere induces a significant enhancement in their performance over time, for both samples with and without additives, although this improvement is retained long-term only for the additive-containing devices. In order to shed light on the photoinduced processes involved, the evolution of the Sn^{+2}/Sn^{+4} and I^-/I_2 ratios of the samples have been tracked by XPS after different light-soaking times (at 1 sun in N_2 atmosphere) from 0 to 15 days (Figure 6B). These ratios have been extracted from the analysis of XPS spectra (Figure S18). As it can be observed, both ratios increased with the illumination reaching their respective maximum values on the third day and later stabilized for longer light-soaking times (4–15 days). The increase of Sn^{+2}/Sn^{+4} ratio with a maximum value after three days of light-soaking is in excellent agreement with the performance improvement upon the illumination presented in Figure S17. This indicates that the main effect of light soaking involves a decrease in the relative amount of Sn^{+4} with respect to Sn^{+2}, which diminishes the defect density and, consequently, enhances the solar cell performance. The question remains to be whether the increase of the surface Sn^{+2}/Sn^{+4} ratio induced by the light-soaking treatment, even observed for the Sn-HP without additives, could be ascribed to the Sn^{+4}/Sn^{+2} photoinduced reduction.

Photoinduced reduction mechanism and the iodine/iodide role

It is well known that heavy metal complexes may display metal-to-ligand or ligand-to-metal charge transfer transitions, MLCT and LMCT, respectively,[68] especially if their intrinsic electron-donor(withdrawing) properties, i.e., redox potentials, are significantly different. This charge transfer processes are often optically active and can be rationalized as intramolecular photoinduced electronic transitions between the metallic center and the ligands or vice versa. Metal halides are clear examples of chemical species that present intense LMCT transitions,[69] and metal iodides are

Please cite this article in press as: Sanchez-Diaz et al., Tin perovskite solar cells with >1,300 h of operational stability in N_2 through a synergistic chemical engineering approach, Joule (2022), https://doi.org/10.1016/j.joule.2022.02.014

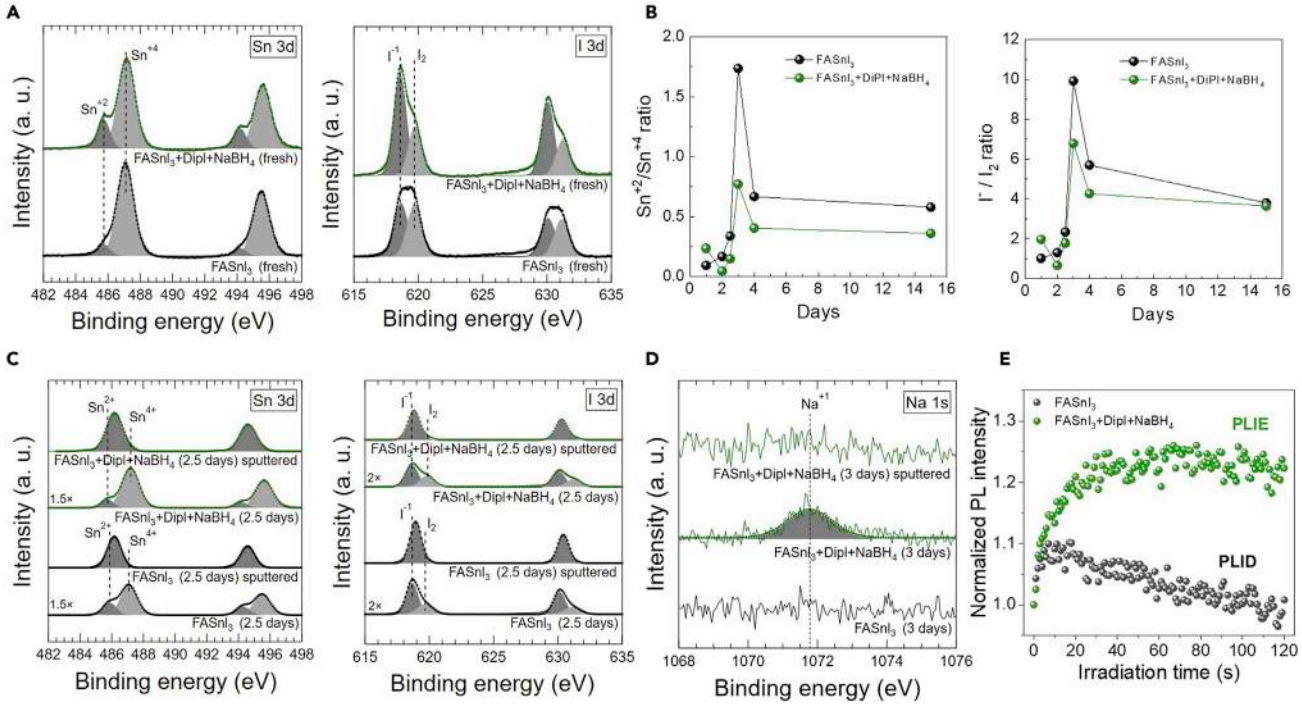

Figure 6. XPS analysis

(A) Sn^{+2}, Sn^{+4} I^-, and I_2 signals obtained from the fresh pristine $FASnI_3$ and $FASnI_3$ + DipI + $NaBH_4$ films, respectively.

(B) Evolution of the Sn^{+2}/Sn^{+4} and I^-/I_2 ratios of both sample compositions upon different illumination times, (X days) indicated for each sample, where X is the light-soaking time at 1 sun in N_2 atmosphere.

(C) Comparison of the Sn^{+2}, Sn^{+4}, I^-, and I_2 signals detected for both Sn-HP compositions before and after surface sputtering.

(D) Na^+ analysis of the films with additives before and after sputtering. The Na^+ content of that sample without additives was also measured as a control.

(E) PL monitorization over the irradiation time for the pristine $FASnI_3$ and $FASnI_3$ + DipI + $NaBH_4$ in vacuum, under continuous excitation (λ_{exc} = 532 nm, 20 mW, light-spot area of 0.07 cm^2).

not an exception. Indeed, SnI_2 and SnI_4 powders show an intense orange color that stems from the optical charge transfer transitions from the iodides to the tin. The LMCT character of all low-energy transitions of the iodo complexes determines their photochemistry. Unlike chloro complexes and as observed in some bromo derivatives, metal iodides undergo a facile intramolecular photo-redox decomposition, which is characteristic of LMCT excitation.[70] Generally, LMCT induces the oxidation of a ligand anion to its radical and a one-electron reduction of the central metal.[68] On the basis of these premises, and considering the higher oxidizing character of the redox pair Sn^{+4}/Sn^{+2} (E°_{red}= +0.15 V versus standard hydrogen electrode [SHE]),[71] or even higher in more recent studies,[72] compared with that of Sn^{+2}/Sn^0 (E°_{red}= −0.14 V versus SHE), the increase of the surface Sn^{+2}/Sn^{+4} ratio is ascribed to the $Sn^{+4} \rightarrow Sn^{+2}$ photoinduced reduction. As shown in Scheme 1 (Reaction A), the Sn^{+2} formation upon the photoreduction of SnI_4 is inherently accompanied with the formation of molecular iodine (I_2) through a radical reaction mechanism.[70] Molecular iodine shows broad vibronic transitions, according to precedents in the literature.[73,74] We have registered the broad absorption signal of I_2 gas in the visible range (λ^{max}_{abs} = 524 nm), which was also identified upon the irradiation of SnI_4 powder in argon at room temperature, as we experimentally demonstrate in Figure S19. These evidences account for the observed evolution of the Sn^{+2}/Sn^{+4} and I^-/I_2 ratios detected for both $FASnI_3$ films (Figure 6B) and reveal the formation of I_2 upon SnI_4 light exposure, a process that is likely to occur also on HP films. In addition, this observation indicates that the evolution of $FASnI_3$ is influenced by the complex

Please cite this article in press as: Sanchez-Diaz et al., Tin perovskite solar cells with >1,300 h of operational stability in N_2 through a synergistic chemical engineering approach, Joule (2022), https://doi.org/10.1016/j.joule.2022.02.014

Reaction A: $SnI_4 + h\nu \rightarrow SnI_2 + I_2$ (in inert atmosphere)

Reaction B:
$$\left.\begin{array}{l} NaBH_4 + I_2 \rightarrow NaI + BH_{3(g)} + HI_{(g)} \\ HI_{(g)} + NaBH_4 \rightarrow NaI + BH_{3(g)} + H_{2(g)} \end{array}\right\} 2\,NaBH_4 + I_2 \rightarrow 2\,NaI + 2\,BH_{3(g)} + H_{2(g)}$$

Scheme 1. Reactivity of the chemical species present in the $FASnI_3$ films

iodine chemistry. The key role of iodine chemistry in the defect formation and behavior for Pb-based perovskite solar cells has been broadly discussed, but its influence on Sn-HP solar cells have received less attention due to the broadly accepted easy oxidation of Sn^{+2} into Sn^{+4} and its main role in defect formation. However, Figure 6B highlights that Sn^{+2}/Sn^{+4} and I^-/I_2 ratios are intimately correlated, and consequently, in order to understand the evolution of the former, it is necessary to examine the reactivity of the later.

To this extent, another interesting and *a priori*, surprising aspect of Figure 6B is that after light soaking, the Sn^{+2}/Sn^{+4} ratio, which is initially higher for the samples with additives, becomes larger for those samples without additives. This fact demands a more detailed analysis because the samples with additives after light soaking still present a higher performance than those without them. It has been reported that I_2 has the tendency to migrate to the surface in Pb halide perovskites,[75,76] where it can sublimate or contribute to the degradation of $FASnI_3$.[77] Note that the loss of I_2 increases I^-/I_2 ratio and unbalance Reaction A in Scheme 1, thus shifting this reaction toward the products and consequently enlarging the Sn^{+2}/Sn^{+4} ratio. This point has been confirmed by storing samples under vacuum in the XPS chamber in order to promote the sublimation of I_2, which induced an increase of both Sn^{+2}/Sn^{+4} and I^-/I_2 ratios (Figure S20). Although this process is expected for both samples with and without additives, the incorporation of additives can influence the iodine chemistry in several ways. Those samples with additives present a decoupled evolution of the chemical ratios whose behavior may arise from several origins. (1) The introduction of DipI might stabilize/passivate the surface blocking the sites where I_2 can migrate.[75] This kind of passivation that affects the iodine interactions has been reported as a key aspect for increasing the performance and stability of Pb-based perovskite solar cells.[75,76] (2) The introduction of the reducing agent opens up a new chemical path (reaction B in Scheme 1). $NaBH_4$ would preferentially reduce the I_2, which is already present in the fresh samples but also potentially photogenerated upon light exposure. Note that the redox potential of the I_2/I^- pair is +0.54 V versus SHE, thus being much higher than that of the Sn^{+4}/Sn^{+2} and Sn^{+2}/Sn^0 redox pairs. In other words, the presence of additives can contribute to passivate and inhibit the loss of iodine species, thus accounting for the lower Sn^{+2}/Sn^{+4} and I^-/I_2 ratios observed in the XPS measurements compared with the pristine $FASnI_3$ samples.

Aimed at proving that the photochemical activity of the additives is mainly located at the HP surface, the samples without and with additives were exposed to 1 sun illumination during 60 h (2.5 days) and sputtered with Ar^+ ions for only 30 s in ultra-high vacuum conditions with the aim of analyzing the inner film compositions. As it can be clearly observed in Figure 6C, the signals corresponding to Sn^{+4} and I_2 are no longer resolved for both sample compositions, thus confirming the capital role of surface in the performance and stability of Sn-based perovskite

Please cite this article in press as: Sanchez-Diaz et al., Tin perovskite solar cells with >1,300 h of operational stability in N_2 through a synergistic chemical engineering approach, Joule (2022), https://doi.org/10.1016/j.joule.2022.02.014

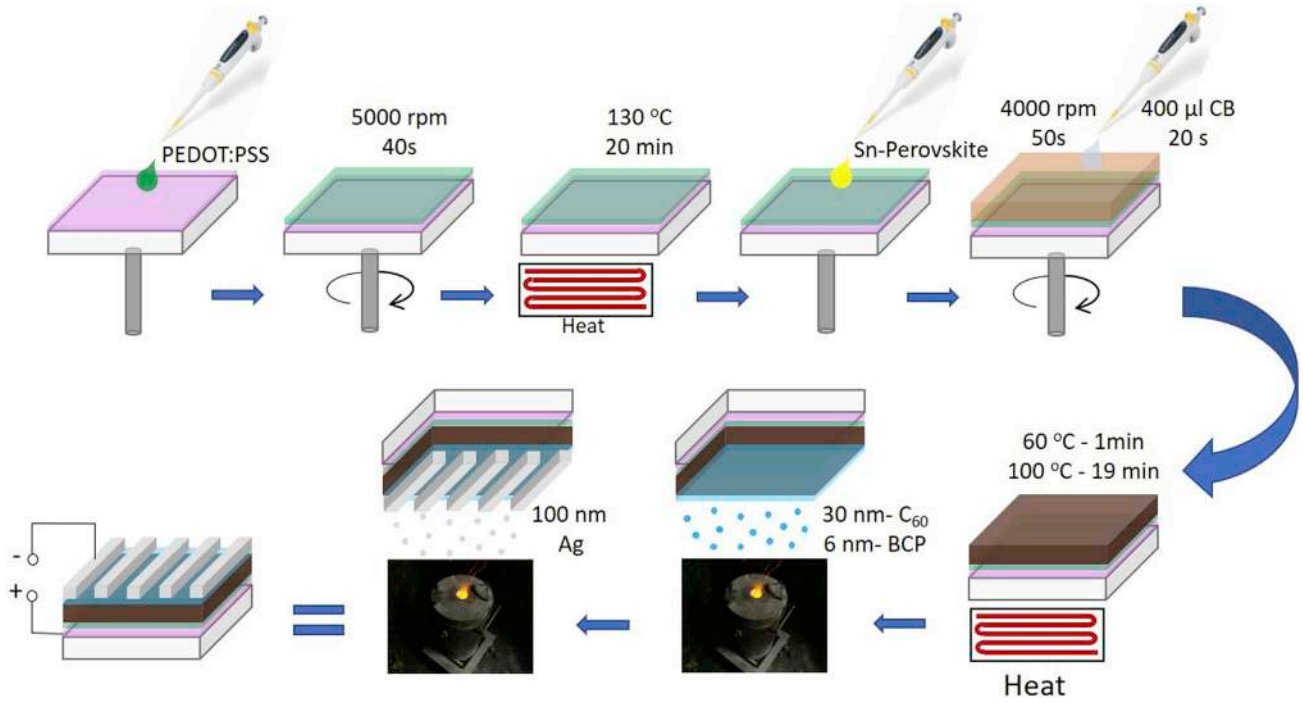

Scheme 2. Schematic illustration of device fabrication procedure steps

solar cells. Interestingly, XPS analysis of the Na^+ content, aimed at detecting the $NaBH_4$, before and after sputtering of the samples with additives, revealed that the alkaline cation is mainly present at the surface of the films (Figure 6D), thus verifying the apparent strong activity of the additives at the semiconductor surface. The pristine $FASnI_3$ film was also analyzed as a control experiment, and as expected, the Na^+ signals were unambiguously not detected.

In order to understand why the samples with additives present a better performance after the light soaking despite the lower Sn^{+2}/Sn^{+4} ratios recorded compared with samples without additives, we monitored the PL signals over time under continuous excitation (see discussion below). Precedent works focused on elucidating the photochemical reactions that occur in Pb-based HP solar cells have reported apparently contradictory results regarding the evolution of the PL over the irradiation time.[78–85] In particular, two significantly different PL behaviors have been historically identified: (1) a PL intensity decrease (PLID) and (2) a PL intensity enhancement (PLIE), whose exact origin seems to be ascribed to the complexity of the photo-electrochemical reactions that occur in the HP-based semiconductor films, which, in turn, depend on the sample processing and measuring conditions, e.g., air versus inert conditions. It is worth mentioning that PLID is unanimously ascribed to photoinduced trap formation, whereas PLIE is understood as a light-induced trap annihilation process, which is also known as healing process.

A recent work[75] correlates the photo-instabilities of the Pb-HP semiconductors/devices with the light-induced formation and annihilation of defects that act as carrier trap states. The authors demonstrate through theoretical modeling and experimental evidence that, depending on the sample properties and/or measuring conditions, e.g., temperature, excitation intensity and wavelength,

both behaviors, PLID and PLIE, can be detected for a given sample. In this regard, we have monitored the PL evolution of our pristine $FASnI_3$ and $FASnI_3$ + DipI + $NaBH_4$ samples. Figure 6E clearly shows that continuous photoexcitation (λ_{exc} = 532 nm) of the $FASnI_3$ films without the incorporation of additives at room temperature in vacuum conditions resulted in a PLID behavior. Contrarily, the $FASnI_3$ + DipI + $NaBH_4$ film displayed a PLIE evolution. According to the precedent work reported by Motti et al.,[75] interstitial iodine (I_i) can significantly trap both electrons and holes through the (+/0) and (0/−) transitions. Hole trapping/de-trapping at I_i^- is a relatively fast process, whereas electron trapping at I_i^+ induces long-living states because the strong associated geometrical relaxation decreases the kinetics of electron de-trapping. This long-living states trigger subsequent photochemical transformations leading to both PLID and PLIE. The recombination of I_i^- with iodine vacancies (V_I^+) has been proposed as a means of $I_i^-V_I^+$ trap annihilation,[80] which restores the initial material and decreases the concentration of traps, thus enhancing the PL. Contrarily, PL quenching is believed to arise from the direct recombination of two interacting I_i^-/I_i^+ defects to give I_2. Importantly, both the coordinated I_2 and the I_i^-/I_i^+ pair tend to migrate to the surface. At this stage, the photogenerated I_2 molecules that, in turn, can trap electrons as I_i^+ do may not only remain bound to the surface or grain boundaries but can also be released as a gas or induce the $FASnI_3$ degradation process.[77] Therefore, the iodine imbalance between surface and bulk can trigger a series of compensating reactions that regenerate the starting equilibrium distribution of I_i^-/I_i^+ defects to compensate their transformation to surface-bound and/or lost I_2, thus contributing to trap formation and successive HP degradation, which justifies the observed PLID and the lower performance and stability of the samples without additives. Note that the passivation of surface sites in the samples with additives prevents the I_2 migration to the surface, and the subsequent imbalance between surface and bulk that triggers the defect formation. It is worth pointing out that our pristine Sn-HP sample shows an initial PL enhancement, roughly during the first 10 s and a subsequent PL quenching at longer irradiation times (Figure 6E), thus revealing a competition between the trap formation and annihilation processes. Hence, we infer that at the initial stage of the pristine $FASnI_3$ PL measurement, as well as for the $FASnI_3$ + DipI + $NaBH_4$ throughout the entire interval time studied, the trap annihilation accounts for the PLIE behavior. By contrast, the $FASnI_3$ film without additives displayed a PLID-like evolution at longer irradiation times (beyond 10 s) that is ascribed to trap formation reactions.

Beyond the degradation mechanisms promoted by O_2 and H_2O,[77] here, we show that iodine chemistry, even in inert atmosphere, plays a key role in the Sn-HP solar cells performance and stability, which also influences the Sn^{+2}/Sn^{+4} composition ratios and gives rise to the light-soaking effect. In addition, PL analysis also points out that iodine trap annihilation and formation processes reported for Pb-HPs could also be present in Sn-HPs. Eventually, additives influence the Sn-HP chemistry by surface passivation, e.g., DipI, and/or introduce additional iodine reactions that balance and fix surface iodine, e.g., $NaBH_4$. These processes are summarized in Figure 7. The different balance of these processes, influenced by the introduction of additives, can explain our experimental results, thus confirming that the incorporation of our additives contributes not only to the diminishment of the defect formation during the fabrication but also to a trap-healing effect at operating conditions, which translates into an enhanced device efficiency and long-term durability.

Please cite this article in press as: Sanchez-Diaz et al., Tin perovskite solar cells with >1,300 h of operational stability in N_2 through a synergistic chemical engineering approach, Joule (2022), https://doi.org/10.1016/j.joule.2022.02.014

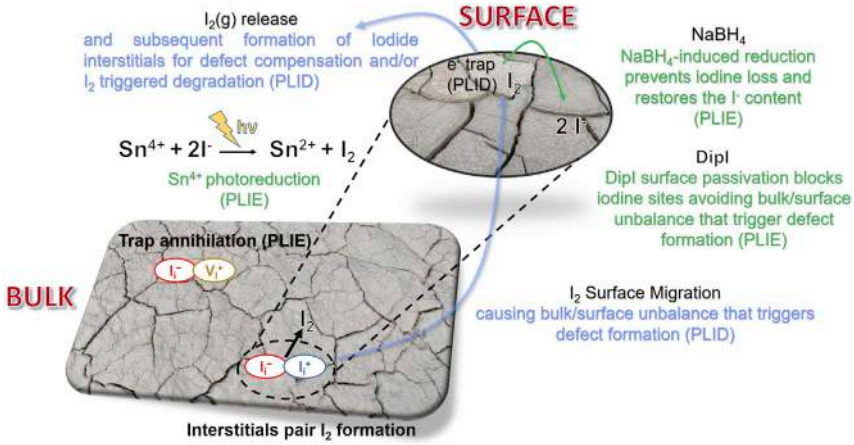

Figure 7. Illustration of the Sn-HP films reactivity under illumination that account for the PLID and PLIE behaviors

The role of $NaBH_4$ (redox mechanism) is crucial to prevent the iodine loss upon gas desorption from the HP surface, which translates into an inhibition of photoinduced trap formation. In the same line, DipI passivation avoids the migration of I_2 to the surface and the subsequent formation of bulk defects to compensate the surface/bulk unbalance.[75] The control of I_2 that triggers the degradation process of $FASnI_3$ into FAI and SnI_4[77] is also dramatic in order to extend the long-term device stability.

Conclusions

This work deals with the handicaps generally encountered during the fabrication of $FASnI_3$ devices compared with the Pb-based counterparts, i.e., reduced *Voc* and limited long-term stability. Our reference devices show a maximum PCE of 6.2% reached upon applying a light-soaking treatment. Unfortunately, the performance of these devices is drastically reduced after approximately 100 h under continuous illumination, even in inert atmosphere. Nevertheless, here, we successfully introduced a novel strategy based on the synergistic combination of two additives, DipI and $NaBH_4$, into the $FASnI_3$ precursor solution, which not only enhanced the efficiency of the devices but also provided a dramatic beneficial impact on the long-term stability. Although the mechanisms might be different, both additives successfully prevent the $Sn^{+2} \rightarrow Sn^{+4}$ oxidation in the precursor solution. In fact, a more significant inhibition is induced when both additives are added. We have demonstrated that $NaBH_4$ has a significant impact on the stability of the Sn-HP films when they are stored in inert conditions. However, the beneficial stabilization of the films prepared with the incorporation of the studied additives was not observed in ambient conditions due to the hydrophilic character of the additives. Nevertheless, the additional stabilization produced by $NaBH_4$ was recovered for completed devices due to the protective effect of perovskite top contact. The observed synergistic effect from the combination of $NaBH_4$ and DipI additives, where the former increases significantly the stability while the latter acts as a surface passivating agent, results in an increase in the photoconversion efficiency, especially after light soaking. As a consequence, the use of $NaBH_4$ and DipI increases the Sn-HP solar cell PCE up to 8.06% and 9.06%, respectively, whereas the combined use of both pushes the solar cell PCE to 10.61%, as the synergistic combination of both additives boosts the *Voc* values upon the light treatment. In addition, outstanding stability levels are reported. In particular, these devices retained 100% of their initial PCE during 5 h under continuous illumination and still maintained 80% after 9 h at MPP in ambient conditions (air at ~60% RH). Likewise, 96% of the initial efficiency was kept after more than 1,300 h under continuous operation at MPP in N_2 atmosphere. To the best of

Please cite this article in press as: Sanchez-Diaz et al., Tin perovskite solar cells with >1,300 h of operational stability in N_2 through a synergistic chemical engineering approach, Joule (2022), https://doi.org/10.1016/j.joule.2022.02.014

our knowledge, these results are unprecedented for unencapsulated Sn-based devices and lead up to the development of outperforming Sn-HP semiconductors. In summary, our strategy allows preparing $FASnI_3$-based devices in a highly reproducible manner that reach long-term stability levels that have not been reported to date. We have systematically characterized our devices in order to understand the origin of the higher performance and stability, as well as the beneficial light-soaking effect in inert atmosphere, independent of the absence or presence of additives. XPS and PL characterization point out the important role of the iodine chemistry in the Sn-HP solar cell performance and stability, which determines the light-soaking effect through Sn^{+4} photoreduction with formation of I_2 that is able to trigger the HP degradation, as well as accounting for the bulk healing effect and trap formation. Therefore, even though the light-soaking treatment induces an unambiguous beneficial impact on the device's performance, it does not seem to be the ultimate solution for further extending the device's lifetime, as it promotes a double side effect. On one hand, it induces a photoreduction of Sn^{+4} species and subsequent trap density diminishment in the bulk and at the interfaces, which is clearly positive. On the other hand, due to the inherent formation of molecular iodine that can act as a charge trap itself, the light-induced ageing also triggers a series of complex halide reactions that may evolve through the formation of new charge traps and drive to premature perovskite degradation. Hence, the exploration of novel strategies that are able to take benefit of the light-soaking effect while controlling the deleterious effect of iodine and their fully mechanistic understanding, similar to the one we report here based on a combination of additives with complementary roles, is required in order to bring the Sn halide perovskites one step beyond.

Consequently, our results unveil the crucial relevance of controlling the photochemistry of halides toward an efficient long-term stabilization of Sn-HP films and devices and indicates the research direction to develop and test more efficient additives to not only provide an efficient passivation but also a thorough control over the halide chemistry. Therefore, this work provides valuable insights into the Sn-based HP solar cells toward further performance and stability improvement, which will pave the way to their eventual introduction into the photovoltaics technology market.

EXPERIMENTAL PROCEDURES

Resource availability

Lead contact

Further information and requests for resources should be directed to and will be fulfilled by the lead contact, Iván Mora Seró (sero@uji.es).

Materials availability

This study did not generate new unique materials.

Data and code availability

The published article and its supplemental information. include all data generated or analyzed during this study.

Materials

Tin(II) iodide (SnI_2, 99.99%), tin(II) fluoride (SnF_2, 99%), bathocuproine (BCP, 99.99%), N,N-dimethylformamide (DMF, 99.8%), and dimethylsulfoxide (DMSO, 99.8%) were purchased from Sigma-Aldrich. PEDOT: PSS Al 4083 aqueous solution was purchased from *Heraeus*. C_{60} (99.95%) was obtained from *Nano-C*. Formamidinium iodide (FAI. 99.99%) was purchased from *Greatcell solar materials*. All materials were use as received with no further purifications.

Please cite this article in press as: Sanchez-Diaz et al., Tin perovskite solar cells with >1,300 h of operational stability in N_2 through a synergistic chemical engineering approach, Joule (2022), https://doi.org/10.1016/j.joule.2022.02.014

Dipropylammonium iodide synthesis

Dipropylammonium iodide salt (DipI) was synthesized following the procedure reported in our previous work.[46] In brief, 10 g Dipropylamine were added to 30 mL of cold EtOH. Then 13 mL of HI were dropwise added to the flask under vigorous stirring. The white solid formed after the addition of HI was filtered and washed with 100 mL of cold diethylether, and it was recrystallized using EtOH.

Preparation of $FASnI_3$ precursor solutions

Pristine $FASnI_3$ precursor solution

298 mg of SnI_2 (0.8 M), 137.57 mg of FAI (0.8 M), and 12.48 mg of SnF_2 (0.08 M) were dissolved in 1 mL of a binary mixture of DMSO:DMF (9:1, v/v) and stirred overnight at room temperature.

$FASnI_3$ precursor solution with $NaBH_4$

298 mg of SnI_2 (0.8 M), 137.57 mg of FAI (0.8 M), 12.48 mg of SnF_2 (0.08 M), and 1.9 mg of $NaBH_4$ (0.05 M) were dissolved in 1 mL of a binary mixture of DMSO:DMF (9:1, v/v) and stirred overnight at room temperature.

$FASnI_3$ precursor solution with DipI

298 mg of SnI_2 (0.8 M), 123.81 mg of FAI (0.72 M), 36.65 mg of DipI (0.16 M), and 12.48 mg of SnF_2 (0.08 M) were dissolved in 1 mL of a binary mixture of DMSO:DMF (9:1, v/v) and stirred overnight at room temperature.

$FASnI_3$ precursor solution with DipI and $NaBH_4$

298 mg of SnI_2 (0.8 M), 123.81 mg of FAI (0.72 M), 36.65 mg of DipI (0.16 M), 12.48 mg of SnF_2 (0.08 M), and 1.9 mg of $NaBH_4$ (0.05 M) were dissolved in 1 mL of a binary mixture of DMSO:DMF (9:1, v/v) and stirred overnight at room temperature.

Device fabrication

ITO coated glass where chemically etched with zinc powder and HCl (6 M) to obtain the desired ITO pattern, followed by a sequential washing process with soap-water, ethanol, acetone, and isopropanol, respectively, in an ultrasonic bath for 15 min each. Then, the substrates were dried with N_2 flow and subsequently introduced in an UV-Ozone lamp for 20 min. The PEDOT:PSS solution was filtered with 0.45 μm PVDF filter and spin coated on top of ITO at 5,000 rpm (2,000 rpm·s^{-1} of acceleration) for 40 s and annealed at 130°C for 20 min in ambient conditions. After the hole transporting layer (HTL) deposition the substrates were introduced in a N_2-filled glovebox, for the $FASnI_3$ layer deposition. The perovskite layer was deposited by one-step method with an anti-solvent-based method, by adding $FASnI_3$ precursor solution (with or without additives) on top of PEDOT:PSS and spin coated at 4,000 rpm for 50 s. Then 400 μL of chlorobenzene were dropped on top of the substrate after 20 s of spinning, followed by a two-step annealing at 70°C for 1 min and at 100°C for 19 min. A 30 nm layer of C_{60} was thermally evaporated on top of the perovskite layer as electron transporting layer (ETL), followed by 6 nm of BCP as buffer layer and 100 nm of Ag as metal contact. Then a light treatment was performed for 3 days under continuous illumination as part of device fabrication. A schematic illustration of device fabrication is shown in Scheme 2.

Film/device characterization

SEM images were taken with a field emission scanning electron microscope (FEG-SEM) JEOL 3100F) operated at 15 kV.

XRD pattern of the films were measured using X-ray diffractometer (D8 Advance, Bruker-AXS) (Cu Kα, wavelength λ = 1.5406 Å) with a Bragg angle range of 4°–70° and step size of 0.05°.

Absorption spectra were registered on a Varian 20Cary300BIO UV/VIS spectrophotometer. The solutions for the absorption measurements were diluted 10 times in order to avoid saturation of the detector. The absorbances of the fresh samples were measured in N_2 atmosphere and then, they were purged with dry air to ensure oxidizing conditions. Upon air purging, the solutions were exposed to 1 sun irradiation with a solar simulator and the absorbance was monitored every 5 min.

J-V curves and MPP in atmosphere conditions, were measured using an Abet technologies (Sun 2,000) solar simulator. The light intensity was adjusted to 1 sun (100 $mW \cdot cm^{-2}$) using a calibrated Si solar cell and a photodiode. The devices were measured in ambient conditions without encapsulation, with an active area of 0.121 cm^2, defined by a mask.

MPP and long-term stability measurements in N_2 conditions were measured under continuous illumination, using a Xenon lamp, by adjusting the sample-light source distance to set an optical power density of 100 $mW \cdot cm^{-2}$, calibrated with a photodiode. The measurements were performed with an AUTOLAB (PGSTAT30) potentiostat; for the long-term stability measurements, an automatic sequence was set to measure the *J-V* curves every 2 h. For the MPP measurements, a fixed voltage corresponding to V_{MPP} was applied, which was obtained from the *J-V* curves, and the electrical current I_{MPP} was monitored over time.

External quantal efficiency (EQE) measurements were performed with a QEPVSI-b Oriel system.

The steady-state PL measurements were registered using an intensified CCD (iStar 320 ICCD/DH320T-25U-03) coupled to a spectrograph (KYMERA-328I-B1) from Andor. A continuous diode-pumped solid-state laser module (532 nm, 150 mW max.) with controllable output power, model GL532RM-150 from SLOC LASERS, was used as an excitation source.

Time-resolved PL (TRPL) of thin films were measured at room temperature in vacuum conditions under excitation by 200 fs pulses from Ti:sapphire laser (Coherent Mira 900D) at a repetition rate of 76 MHz doubled to 405 nm with a BBO crystal. The backscattered PL signal was dispersed by a double 0.3-m focal length grating spectrograph/spectrometer (1,200 g/mm with 750 nm blaze) and detected by a Si micro photon device (MPD) and single-photon avalanche diode (SPAD) photodetector (connected through a multimode optical fiber to the monochromator); the SPAD was attached to a time correlated single photon counting electronic board (TCC900 from Edinburgh Instruments). The excitation fluence is 15 $nJ \cdot cm^{-2}$, the instrument response function (IRF) is about 50 ps.

XPS measurements were performed in a SPECS GmbH system (base pressure 1.0×10^{-10} mbar) equipped with a PHOIBOS 150 2D-CMOS hemispherical analyzer. Photoelectrons were excited with the Al-Ka line (1,486.7 eV) of a monochromatic X-ray source μ-FOCUS 500 (SPECS GmbH). Measurements were taken at room temperature with a pass-energy of 20 eV. To study depth profiles by XPS, some of the samples were sputtered by 30 s using an IQE 11/35 3 kV Ar^+ source. Sample stability was also

studied by XPS. To perform this study, some samples were characterized by XPS and kept in dark under ultra-high-vacuum conditions for 15 days, repeating then the XPS analysis.

SUPPLEMENTAL INFORMATION

Supplemental information can be found online at https://doi.org/10.1016/j.joule.2022.02.014.

ACKNOWLEDGMENTS

This work was made possible by the Horizon 2020 research and innovation program through the DROP-IT project (grant agreement no. 862656) and MSCA Innovative Training Network (grant agreement no. 764787), the Ministry of Science and Innovation of Spain under project STABLE PID2019-107314RB-I00, the European Research Council (ERC) via Consolidator Grant (724424 - No-LIMIT), and the University Jaume I (project DEPE2D UJI-B2019-09).

AUTHOR CONTRIBUTIONS

J.S.-D., R.S.S., and I.M.-S. conceived the idea, oversaw the project, and wrote the manuscript. J.S.-D. carried out device fabrication and characterization. R.S.S. designed and performed the UV-Vis characterization in solution and in gas phase and substantially contributed to the rationalization of the overall experimental results and developed most of the (photo-)(electro-)chemical mechanistic interpretation. S.M. assisted with some characterization ideas and SEM characterization. A.O.A. designed the measuring program and registered the *MPP* and long-term device's measurements. M.K. and J.F.S.-R. registered the XPS measurements and aided in interpreting the data. E.M.B. carried out the AFM experiments. J.R.R. synthesized and characterized the DipI precursor. V.S.C. and J.P.M.-P. carried out TRPL measurements. All the authors are involved in the discussion on data analysis and contributed to manuscript preparation. I.M.-S. coordinated the work.

DECLARATION OF INTERESTS

The authors declare no competing interests.

Received: September 8, 2021
Revised: October 29, 2021
Accepted: February 18, 2022
Published: March 14, 2022

REFERENCES

1. Lee, M.M., Teuscher, J., Miyasaka, T., Murakami, T.N., and Snaith, H.J. (2012). Efficient hybrid solar cells based on meso-superstructured organometal halide perovskites. Science *338*, 643–647. https://doi.org/10.1126/science.1228604.

2. Kojima, A., Teshima, K., Shirai, Y., and Miyasaka, T. (2009). Organometal halide perovskites as visible-light sensitizers for photovoltaic cells. J. Am. Chem. Soc. *131*, 6050–6051. https://doi.org/10.1021/ja809598r.

3. Kim, H.S., Lee, C.R., Im, J.H., Lee, K.B., Moehl, T., Marchioro, A., Moon, S.J., Humphry-Baker, R., Yum, J.H., Moser, J.E., et al. (2012). Lead iodide perovskite sensitized all-solid-state submicron thin film mesoscopic solar cell with efficiency exceeding 9%. Sci. Rep. *2*, 591. https://doi.org/10.1038/srep00591.

4. Min, H., Kim, M., Lee, S.U., Kim, H., Kim, G., Choi, K., Lee, J.H., and Seok, S.I. (2019). Efficient, stable solar cells by using inherent bandgap of α-phase formamidinium lead iodide. Science *366*, 749–753. https://doi.org/10.1126/science.aay7044.

5. National Renewable Energy Laboratory (2021). Best research-cell efficiencies. https://www.nrel.gov/pv/cell-efficiency.html.

6. Jeong, J., Kim, M., Seo, J., Lu, H., Ahlawat, P., Mishra, A., Yang, Y., Hope, M.A., Eickemeyer, F.T., Kim, M., et al. (2021). Pseudo-halide anion engineering for α- $FAPbI_3$ perovskite solar cells. Nature *592*, 381–385. https://doi.org/10.1038/s41586-021-03406-5.

7. Lyu, M., Yun, J.H., Chen, P., Hao, M., and Wang, L. (2017). Addressing toxicity of lead: progress and applications of low-toxic metal halide perovskites and their derivatives. Adv. Energy Mater. *7*, 1602512. https://doi.org/10.1002/aenm.201602512.

8. Flora, G., Gupta, D., and Tiwari, A. (2012). Toxicity of lead: a review with recent updates. Interdiscip. Toxicol. *5*, 47–58. https://doi.org/10.2478/v10102-012-0009-2.

9. Slavney, A.H., Smaha, R.W., Smith, I.C., Jaffe, A., Umeyama, D., and Karunadasa, H.I. (2017). Chemical approaches to addressing the instability and toxicity of lead–halide

perovskite absorbers. Inorg. Chem. *56*, 46–55. https://doi.org/10.1021/acs.inorgchem.6b01336.

10. Saparov, B., Hong, F., Sun, J.-P., Duan, H.-S., Meng, W., Cameron, S., Hill, I.G., Yan, Y., and Mitzi, D.B. (2015). Thin-film preparation and characterization of $Cs_3Sb_2I_9$: a lead-free layered perovskite semiconductor. Chem. Mater. *27*, 5622–5632. https://doi.org/10.1021/acs.chemmater.5b01989.

11. Bai, F., Hu, Y., Hu, Y., Qiu, T., Miao, X., and Zhang, S. (2018). Lead-free, air-stable ultrathin Cs3Bi2I9 perovskite nanosheets for solar cells. Sol. Energy Mater. Sol. Cells *184*, 15–21. https://doi.org/10.1016/j.solmat.2018.04.032.

12. Cortecchia, D., Dewi, H.A., Yin, J., Bruno, A., Chen, S., Baikie, T., Boix, P.P., Grätzel, M., Mhaisalkar, S., Soci, C., and Mathews, N. (2016). Lead-free MA2CuCl(x)Br(4-x) hybrid perovskites. Inorg. Chem. *55*, 1044–1052. https://doi.org/10.1021/acs.inorgchem.5b01896.

13. Krishnamoorthy, T., Ding, H., Yan, C., Leong, W.L., Baikie, T., Zhang, Z., Sherburne, M., Li, S., Asta, M., Mathews, N., and Mhaisalkar, S.G. (2015). Lead-free germanium iodide perovskite materials for photovoltaic applications. J. Mater. Chem. A *3*, 23829–23832. https://doi.org/10.1039/C5TA05741H.

14. Noel, N.K., Stranks, S.D., Abate, A., Wehrenfennig, C., Guarnera, S., Haghighirad, A.-A., Sadhanala, A., Eperon, G.E., Pathak, S.K., Johnston, M.B., et al. (2014). Lead-free organic–inorganic tin halide perovskites for photovoltaic applications. Energy Environ. Sci. *7*, 3061–3068. https://doi.org/10.1039/C4EE01076K.

15. Li, J., Cao, H.-L., Jiao, W.-B., Wang, Q., Wei, M., Cantone, I., Lü, J., and Abate, A. (2020). Biological impact of lead from halide perovskites reveals the risk of introducing a safe threshold. Nat. Commun. *11*, 310. https://doi.org/10.1038/s41467-019-13910-y.

16. Mitzi, D.B., Feild, C.A., Schlesinger, Z., and Laibowitz, R.B. (1995). Transport, optical, and magnetic properties of the conducting halide perovskite $CH_3NH_3SnI_3$. J. Solid State Chem. *114*, 159–163. https://doi.org/10.1006/jssc.1995.1023.

17. Takahashi, Y., Hasegawa, H., Takahashi, Y., and Inabe, T. (2013). Hall mobility in tin iodide perovskite $CH_3NH_3SnI_3$: evidence for a doped semiconductor. J. Solid State Chem. *205*, 39–43. https://doi.org/10.1016/j.jssc.2013.07.008.

18. Chung, I., Song, J.-H., Im, J., Androulakis, J., Malliakas, C.D., Li, H., Freeman, A.J., Kenney, J.T., and Kanatzidis, M.G. (2012). $CsSnI_3$: semiconductor or metal? High electrical conductivity and strong near-infrared photoluminescence from a single material. High hole mobility and phase-transitions. J. Am. Chem. Soc. *134*, 8579–8587. https://doi.org/10.1021/ja301539s.

19. Ke, W., and Kanatzidis, M.G. (2019). Prospects for low-toxicity lead-free perovskite solar cells. Nat. Commun. *10*, 965. https://doi.org/10.1038/s41467-019-08918-3.

20. Filippetti, A., Kahmann, S., Caddeo, C., Mattoni, A., Saba, M., Bosin, A., and Loi, M.A. (2021). Fundamentals of tin iodide perovskites: a promising route to highly efficient, lead-free solar cells. J. Mater. Chem. A *9*, 11812–11826. https://doi.org/10.1039/D1TA01573G.

21. Liu, F., Marongiu, D., Pau, R., Sarritzu, V., Wang, Q., Lai, S., Lehmann, A.G., Quochi, F., Saba, M., Mura, A., et al. (2020). Ag/In lead-free double perovskites. EcoMat *2*, e12017. https://doi.org/10.1002/eom2.12017.

22. Jin, Z., Zhang, Z., Xiu, J., Song, H., Gatti, T., and He, Z. (2020). A critical review on bismuth and antimony halide based perovskites and their derivatives for photovoltaic applications: recent advances and challenges. J. Mater. Chem. A *8*, 16166–16188. https://doi.org/10.1039/D0TA05433J.

23. Nishimura, K., Kamarudin, M.A., Hirotani, D., Hamada, K., Shen, Q., Iikubo, S., Minemoto, T., Yoshino, K., and Hayase, S. (2020). Lead-free tin-halide perovskite solar cells with 13% efficiency. Nano Energy *74*, 104858. https://doi.org/10.1016/j.nanoen.2020.104858.

24. Wang, C., Zhang, Y., Gu, F., Zhao, Z., Li, H., Jiang, H., Bian, Z., and Liu, Z. (2021). Illumination durability and high-efficiency Sn-based perovskite solar cell under coordinated control of phenylhydrazine and halogen ions. Matter *4*, 709–721. https://doi.org/10.1016/j.matt.2020.11.012.

25. Jiang, X., Li, H., Zhou, Q., Wei, Q., Wei, M., Jiang, L., Wang, Z., Peng, Z., Wang, F., Zang, Z., et al. (2021). One-step synthesis of SnI_2·(DMSO)x adducts for high-performance tin perovskite solar cells. J. Am. Chem. Soc. *143*, 10970–10976. https://doi.org/10.1021/jacs.1c03032.

26. Wang, N., Zhou, Y., Ju, M.G., Garces, H.F., Ding, T., Pang, S., Zeng, X.C., Padture, N.P., and Sun, X.W. (2016). Heterojunction-depleted lead-free perovskite solar cells with coarse-grained B-γ-CsSnI3 thin films. Adv. Energy Mater. *6*, 1601130. https://doi.org/10.1002/aenm.201601130.

27. Kumar, M.H., Dharani, S., Leong, W.L., Boix, P.P., Prabhakar, R.R., Baikie, T., Shi, C., Ding, H., Ramesh, R., Asta, M., et al. (2014). Lead-free halide perovskite solar cells with high photocurrents realized through vacancy modulation. Adv. Mater. *26*, 7122–7127. https://doi.org/10.1002/adma.201401991.

28. He, X., Wu, T., Liu, X., Wang, Y., Meng, X., Wu, J., Noda, T., Yang, X., Moritomo, Y., Segawa, H., and Han, L. (2020). Highly efficient tin perovskite solar cells achieved in a wide oxygen concentration range. J. Mater. Chem. A *8*, 2760–2768. https://doi.org/10.1039/C9TA13159K.

29. Di Girolamo, D., Pascual, J., Aldamasy, M.H., Iqbal, Z., Li, G., Radicchi, E., Li, M., Turren-Cruz, S.-H., Nasti, G., Dallmann, A., et al. (2021). Solvents for processing stable tin halide perovskites. ACS Energy Lett. *6*, 959–968. https://doi.org/10.1021/acsenergylett.0c02656.

30. Wang, T., Tai, Q., Guo, X., Cao, J., Liu, C.-K., Wang, N., Shen, D., Zhu, Y., Lee, C.-S., and Yan, F. (2020). Highly air-stable tin-based perovskite solar cells through grain-surface protection by gallic acid. ACS Energy Lett. *5*, 1741–1749. https://doi.org/10.1021/acsenergylett.0c00526.

31. Li, W., Li, J., Li, J., Fan, J., Mai, Y., and Wang, L. (2016). Addictive-assisted construction of all-inorganic CsSnIBr2 mesoscopic perovskite solar cells with superior thermal stability up to 473 K. J. Mater. Chem. A *4*, 17104–17110. https://doi.org/10.1039/C6TA08332C.

32. Gupta, S., Bendikov, T., Hodes, G., and Cahen, D. (2016). $CsSnBr_3$, A lead-free halide perovskite for long-term solar cell application: insights on SnF_2 addition. ACS Energy Lett. *1*, 1028–1033. https://doi.org/10.1021/acsenergylett.6b00402.

33. Lee, S.J., Shin, S.S., Kim, Y.C., Kim, D., Ahn, T.K., Noh, J.H., Seo, J., and Seok, S.I. (2016). Fabrication of efficient formamidinium tin iodide perovskite solar cells through SnF_2–Pyrazine complex. J. Am. Chem. Soc. *138*, 3974–3977. https://doi.org/10.1021/jacs.6b00142.

34. Tsai, C.M., Mohanta, N., Wang, C.Y., Lin, Y.P., Yang, Y.W., Wang, C.L., Hung, C.H., and Diau, E.W.G. (2017). Formation of Stable Tin Perovskites Co-crystallized with three halides for carbon-based mesoscopic lead-free perovskite solar cells. Angew. Chem. Int. Ed. Engl. *56*, 13819–13823. https://doi.org/10.1002/anie.201707037.

35. Gu, F., Ye, S., Zhao, Z., Rao, H., Liu, Z., Bian, Z., and Huang, C. (2018). Improving performance of lead-free formamidinium tin triiodide perovskite solar cells by tin source purification. Sol. RRL *2*, 1800136. https://doi.org/10.1002/solr.201800136.

36. Wang, C., Gu, F., Zhao, Z., Rao, H., Qiu, Y., Cai, Z., Zhan, G., Li, X., Sun, B., Yu, X., et al. (2020). Self-repairing tin-based perovskite solar cells with a breakthrough efficiency over 11%. Adv. Mater. *32*, e1907623. https://doi.org/10.1002/adma.201907623.

37. Chen, K., Wu, P., Yang, W., Su, R., Luo, D., Yang, X., Tu, Y., Zhu, R., and Gong, Q. (2018). Low-dimensional perovskite interlayer for highly efficient lead-free formamidinium tin iodide perovskite solar cells. Nano Energy *49*, 411–418. https://doi.org/10.1016/j.nanoen.2018.05.006.

38. Li, P., Dong, H., Xu, J., Chen, J., Jiao, B., Hou, X., Li, J., and Wu, Z. (2020). Ligand orientation-induced lattice robustness for highly efficient and stable tin-based perovskite solar cells. ACS Energy Lett. *5*, 2327–2334. https://doi.org/10.1021/acsenergylett.0c00960.

39. Wang, F., Jiang, X., Chen, H., Shang, Y., Liu, H., Wei, J., Zhou, W., He, H., Liu, W., and Ning, Z. (2018). 2D-Quasi-2D-3D hierarchy structure for tin perovskite solar cells with enhanced efficiency and stability. Joule *2*, 2732–2743. https://doi.org/10.1016/j.joule.2018.09.012.

40. Jokar, E., Chien, C.-H., Fathi, A., Rameez, M., Chang, Y.-H., and Diau, E.W.-G. (2018). Slow surface passivation and crystal relaxation with additives to improve device performance and durability for tin-based perovskite solar cells. Energy Environ. Sci. *11*, 2353–2362. https://doi.org/10.1039/C8EE00956B.

41. Liao, Y., Liu, H., Zhou, W., Yang, D., Shang, Y., Shi, Z., Li, B., Jiang, X., Zhang, L., Quan, L.N., et al. (2017). Highly oriented low-dimensional tin halide perovskites with enhanced stability and photovoltaic performance. J. Am. Chem.

Soc. *139*, 6693–6699. https://doi.org/10.1021/jacs.7b01815.

42. Liu, X., Wu, T., Chen, J.-Y., Meng, X., He, X., Noda, T., Chen, H., Yang, X., Segawa, H., Wang, Y., and Han, L. (2020). Templated growth of $FASnI_3$ crystals for efficient tin perovskite solar cells. Energy Environ. Sci. *13*, 2896–2902. https://doi.org/10.1039/D0EE01845G.

43. Li, M., Zuo, W.-W., Yang, Y.-G., Aldamasy, M.H., Wang, Q., Cruz, S.H.T., Feng, S.-L., Saliba, M., Wang, Z.-K., and Abate, A. (2020). Tin halide perovskite films made of highly oriented 2D crystals enable more efficient and stable lead-free perovskite solar cells. ACS Energy Lett. *5*, 1923–1929. https://doi.org/10.1021/acsenergylett.0c00782.

44. Liao, M., Yu, B.-B., Jin, Z., Chen, W., Zhu, Y., Zhang, X., Yao, W., Duan, T., Djerdj, I., and He, Z.J.C. (2019). Efficient and stable FASnI3 perovskite solar cells with effective interface modulation by low-dimensional perovskite layer. ChemSusChem *12*, 5007–5014. https://doi.org/10.1002/cssc.201902000.

45. Chen, M., Dong, Q., Eickemeyer, F.T., Liu, Y., Dai, Z., Carl, A.D., Bahrami, B., Chowdhury, A.H., Grimm, R.L., Shi, Y., et al. (2020). High-performance lead-free solar cells based on tin-halide perovskite thin films functionalized by a divalent organic cation. ACS Energy Lett. *5*, 2223–2230. https://doi.org/10.1021/acsenergylett.0c00888.

46. Rodríguez-Romero, J., Sanchez-Diaz, J., Echeverría-Arrondo, C., Masi, S., Esparza, D., Barea, E.M., and Mora-Seró, I. (2020). Widening the 2D/3D perovskite family for efficient and thermal-resistant solar cells by the use of secondary ammonium cations. ACS Energy Lett. *5*, 1013–1021. https://doi.org/10.1021/acsenergylett.9b02755.

47. Diau, E.W.-G., Jokar, E., and Rameez, M. (2019). Strategies to improve performance and stability for tin-based perovskite solar cells. ACS Energy Lett. *4*, 1930–1937. https://doi.org/10.1021/acsenergylett.9b01179.

48. Xu, L., Feng, X., Jia, W., Lv, W., Mei, A., Zhou, Y., Zhang, Q., Chen, R.-F., and Huang, W. (2021). Recent advances in inverted lead-free tin-based perovskite solar cells and challenges. Energy Environ. Sci. *14*, 4292–4317. https://doi.org/10.1039/D1EE00890K.

49. Jokar, E., Chien, C.-H., Tsai, C.-M., Fathi, A., and Diau, E.W.-G. (2019). Robust tin-based perovskite solar cells with hybrid organic cations to attain efficiency approaching 10%. Adv. Mater. *31*, e1804835. https://doi.org/10.1002/adma.201804835.

50. Hao, F., Stoumpos, C.C., Guo, P., Zhou, N., Marks, T.J., Chang, R.P.H., and Kanatzidis, M.G. (2015). Solvent-mediated crystallization of CH3NH3SnI3 films for heterojunction depleted perovskite solar cells. J. Am. Chem. Soc. *137*, 11445–11452. https://doi.org/10.1021/jacs.5b06658.

51. Pascual, J., Nasti, G., Aldamasy, M.H., Smith, J.A., Flatken, M., Phung, N., Di Girolamo, D., Turren-Cruz, S.-H., Li, M., Dallmann, A., et al. (2020). Origin of Sn(ii) oxidation in tin halide perovskites. Mater. Adv. *1*, 1066–1070. https://doi.org/10.1039/D0MA00245C.

52. Hao, F., Stoumpos, C.C., Cao, D.H., Chang, R.P.H., and Kanatzidis, M.G. (2014). Lead-free solid-state organic–inorganic halide perovskite solar cells. Nat. Photonics *8*, 489–494. https://doi.org/10.1038/nphoton.2014.82.

53. Shao, S., Liu, J., Portale, G., Fang, H.-H., Blake, G.R., ten Brink, G.H., Koster, L.J.A., and Loi, M.A. (2018). Highly reproducible Sn-based hybrid perovskite solar cells with 9% efficiency. Adv. Energy Mater. *8*, 1702019. https://doi.org/10.1002/aenm.201702019.

54. Saidaminov, M.I., Spanopoulos, I., Abed, J., Ke, W., Wicks, J., Kanatzidis, M.G., and Sargent, E.H. (2020). Conventional solvent oxidizes Sn(II) in perovskite inks. ACS Energy Lett. *5*, 1153–1155. https://doi.org/10.1021/acsenergylett.0c00402.

55. Leijtens, T., Prasanna, R., Gold-Parker, A., Toney, M.F., and McGehee, M.D. (2017). Mechanism of tin oxidation and stabilization by lead substitution in tin halide perovskites. ACS Energy Lett. *2*, 2159–2165. https://doi.org/10.1021/acsenergylett.7b00636.

56. Liu, B., Soe, C.M.M., Stoumpos, C.C., Nie, W., Tsai, H., Lim, K., Mohite, A.D., Kanatzidis, M.G., Marks, T.J., and Singer, K.D. (2017). Optical properties and modeling of 2D perovskite solar cells. Sol. RRL *1*, 1700062. https://doi.org/10.1002/solr.201700062.

57. Zhang, T., Dar, M.I., Li, G., Xu, F., Guo, N., Grätzel, M., and Zhao, Y. (2017). Bication lead iodide 2D perovskite component to stabilize inorganic α-CsPbI3 perovskite phase for high-efficiency solar cells. Sci. Adv. *3*, e1700841. https://doi.org/10.1126/sciadv.1700841.

58. Handa, T., Aharen, T., Wakamiya, A., and Kanemitsu, Y. (2018). Radiative recombination and electron-phonon coupling in lead-free $CH3NH3SnI_3$ perovskite thin films. Phys. Rev. Mater. *2*, 075402. https://doi.org/10.1103/PhysRevMaterials.2.075402.

59. Cao, J., and Yan, F. (2021). Recent progress in tin-based perovskite solar cells. Energy Environ. Sci. *14*, 1286–1325. https://doi.org/10.1039/D0EE04007J.

60. Sze, S.M., Li, Y., and Ng, K.K. (2021). Physics of Semiconductor Devices (John Wiley & Sons).

61. Milot, R.L., Klug, M.T., Davies, C.L., Wang, Z., Kraus, H., Snaith, H.J., Johnston, M.B., and Herz, L.M. (2018). The effects of doping density and temperature on the optoelectronic properties of formamidinium tin triiodide thin films. Adv. Mater. *30*, e1804506. https://doi.org/10.1002/adma.201804506.

62. Baig, F., Khattak, Y.H., Marí, B., Beg, S., Ahmed, A., and Khan, K. (2018). Efficiency enhancement of $CH3NH3SnI_3$ solar cells by device modeling. J. Electron. Mater. *47*, 5275–5282. https://doi.org/10.1007/s11664-018-6406-3.

63. Xu, S., Liu, G., Zheng, H., Xu, X., Zhang, L., Xu, H., Zhu, L., Kong, F., Li, Y., and Pan, X. (2020). Boosting photovoltaic performance and stability of super-halogen-substituted perovskite solar cells by simultaneous methylammonium immobilization and vacancy compensation. ACS Appl. Mater. Interfaces *12*, 8249–8259. https://doi.org/10.1021/acsami.9b21074.

64. Alvarez, A.O., Arcas, R., Aranda, C.A., Bethencourt, L., Mas-Marzá, E., Saliba, M., and Fabregat-Santiago, F. (2020). Negative capacitance and inverted hysteresis: matching features in perovskite solar cells. J. Phys. Chem. Lett. *11*, 8417–8423. https://doi.org/10.1021/acs.jpclett.0c02331.

65. Snaith, H.J., Abate, A., Ball, J.M., Eperon, G.E., Leijtens, T., Noel, N.K., Stranks, S.D., Wang, J.T.-W., Wojciechowski, K., and Zhang, W. (2014). Anomalous hysteresis in perovskite solar cells. J. Phys. Chem. Lett. *5*, 1511–1515. https://doi.org/10.1021/jz500113x.

66. Shao, Y., Fang, Y., Li, T., Wang, Q., Dong, Q., Deng, Y., Yuan, Y., Wei, H., Wang, M., Gruverman, A., et al. (2016). Grain boundary dominated ion migration in polycrystalline organic–inorganic halide perovskite films. Energy Environ. Sci. *9*, 1752–1759. https://doi.org/10.1039/C6EE00413J.

67. Liu, X., Wang, Y., Wu, T., He, X., Meng, X., Barbaud, J., Chen, H., Segawa, H., Yang, X., and Han, L. (2020). Efficient and stable tin perovskite solar cells enabled by amorphous-polycrystalline structure. Nat. Commun. *11*, 2678. https://doi.org/10.1038/s41467-020-16561-6.

68. Perutz, R.N. (1994). In Photosensitation and Photocatalysis Using Inorganic and Organic Compounds, K. Kalyanasundarum and M. Grätzel, eds. (Kluwer Academic Publishers).

69. Mo, C.-J., Li, Z.-Q., Que, C.-J., Zhang, G.-L., Zhu, Q.-Y., and Dai, J. (2017). Composition dependent structural, optical and photosensitive properties of a series of charge-transfer tin halides. Dyes Pigment *141*, 66–73. https://doi.org/10.1016/j.dyepig.2017.01.073.

70. Oldenburg, K., Vogler, A., Mikó, I., and Horváth, O. (1996). Photoredox decomposition of tin(II), lead(II), antimony(III) and bismuth(III) iodide complexes in solution. Inorg. Chim. Acta *248*, 107–110. https://doi.org/10.1016/0020-1693(95)04980-0.

71. Latimer, W.M. (1938). Oxidation States of the Elements and Their Potentials in Aqueous Solutions (Prentice-Hall, Inc.).

72. Gajda, T., Sipos, P., and Gamsjäger, H. (2009). The standard electrode potential of the Sn4+/Sn2+ couple revisited. Mon. Chem *140*, 1293–1303.

73. Cooper, P.D. (2010). A simple and convenient method of multiple linear regression to calculate iodine molecular constants. J. Chem. Educ. *87*, 687–690. https://doi.org/10.1021/ed100287r.

74. Evans, D.F. (1955). Absorption spectra of iodine and bromine in the gas phase and ''inert'' solvents. I. Iodine. J. Chem. Phys. *23*, 1424–1426.

75. Motti, S.G., Meggiolaro, D., Barker, A.J., Mosconi, E., Perini, C.A.R., Ball, J.M., Gandini, M., Kim, M., De Angelis, F., and Petrozza, A. (2019). Controlling competing photochemical reactions stabilizes perovskite solar cells. Nat. Photonics *13*, 532–539. https://doi.org/10.1038/s41566-019-0435-1.

76. Meggiolaro, D., Motti, S.G., Mosconi, E., Barker, A.J., Ball, J., Andrea Riccardo Perini, C.,

Deschler, F., Petrozza, A., and De Angelis, F. (2018). Iodine chemistry determines the defect tolerance of lead-halide perovskites. Energy Environ. Sci. *11*, 702–713. https://doi.org/10.1039/C8EE00124C.

77. Lanzetta, L., Webb, T., Zibouche, N., Liang, X., Ding, D., Min, G., Westbrook, R.J.E., Gaggio, B., Macdonald, T.J., Islam, M.S., and Haque, S.A. (2021). Degradation mechanism of hybrid tin-based perovskite solar cells and the critical role of tin (IV) iodide. Nat. Commun. *12*, 2853. https://doi.org/10.1038/s41467-021-22864-z.

78. Kim, G.Y., Senocrate, A., Yang, T.-Y., Gregori, G., Grätzel, M., and Maier, J. (2018). Large tunable photoeffect on ion conduction in halide perovskites and implications for photodecomposition. Nat. Mater. *17*, 445–449. https://doi.org/10.1038/s41563-018-0038-0.

79. deQuilettes, D.W., Zhang, W., Burlakov, V.M., Graham, D.J., Leijtens, T., Osherov, A., Bulović, V., Snaith, H.J., Ginger, D.S., and Stranks, S.D. (2016). Photo-induced halide redistribution in organic–inorganic perovskite films. Nat. Commun. *7*, 11683. https://doi.org/10.1038/ncomms11683.

80. Mosconi, E., Meggiolaro, D., Snaith, H.J., Stranks, S.D., and De Angelis, F. (2016). Light-induced annihilation of Frenkel defects in organo-lead halide perovskites. Energy Environ. Sci. *9*, 3180–3187. https://doi.org/10.1039/C6EE01504B.

81. Xing, J., Wang, Q., Dong, Q., Yuan, Y., Fang, Y., and Huang, J. (2016). Ultrafast ion migration in hybrid perovskite polycrystalline thin films under light and suppression in single crystals. Phys. Chem. Chem. Phys. *18*, 30484–30490. https://doi.org/10.1039/C6CP06496E.

82. Motti, S.G., Gandini, M., Barker, A.J., Ball, J.M., Srimath Kandada, A.R., and Petrozza, A. (2016). Photoinduced emissive trap states in lead halide perovskite semiconductors. ACS Energy Lett. *1*, 726–730. https://doi.org/10.1021/acsenergylett.6b00355.

83. Hong, D., Zhou, Y., Wan, S., Hu, X., Xie, D., and Tian, Y.J.A.P. (2018). Nature of photoinduced quenching traps in methylammonium lead triiodide perovskite revealed by reversible photoluminescence decline. ACS Photonics *5*, 2034–2043. https://doi.org/10.1021/acsphotonics.7b01537.

84. Stranks, S.D., Burlakov, V.M., Leijtens, T., Ball, J.M., Goriely, A., and Snaith, H.J. (2014). Recombination kinetics in organic-inorganic perovskites: excitons, free charge, and subgap states. Phys. Rev. Appl. *2*, 034007. https://doi.org/10.1103/PhysRevApplied.2.034007.

85. Chen, S., Wen, X., Huang, S., Huang, F., Cheng, Y.-B., Green, M., and Ho-Baillie, A. (2017). Light illumination induced photoluminescence enhancement and quenching in lead halide perovskite. Sol. RRL *1*. https://doi.org/10.1002/solr.201600001.

Joule, Volume *6*

Supplemental information

Tin perovskite solar cells with >1,300 h of operational stability in N_2 through a synergistic chemical engineering approach

Jesús Sanchez-Diaz, Rafael S. Sánchez, Sofia Masi, Marie Krečmarová, Agustín O. Alvarez, Eva M. Barea, Jesús Rodriguez-Romero, Vladimir S. Chirvony, Juan F. Sánchez-Royo, Juan P. Martinez-Pastor, and Iván Mora-Seró

SUPPLEMENTAL INFORMATION

SUPPLEMENTAL EXPERIMENTAL PROCEDURES

Preliminary optimization of SnI_2 and additive's concentrations

In an initial stage of this research we optimized the DipI and $NaBH_4$ additive's concentrations. The averaged cell parameters corresponding to devices with the different DipI/FAI ratios before and after a 4-hours light-soaking treatment in ambient conditions are displayed on Table S1 and S2, respectively. As it can be clearly seen, the fresh device's performances do not seem to be extremely influenced by the DipI content (Table S1), within the studied range; however, upon exposure to light the behavior is notably different. While the n=10 sample yielded a +4.7% *PCE* enhancement, the other compositions experienced a decrease in their performances (Table S2). Due to the slightly superior performance of the devices, we fixed the DipI content to n=10 with the aim of narrowing the number of variables throughout the device's optimization process, that corresponds to a DipI:FA mol ratio of 2:9.

Table S1. Averaged cell parameters of the fresh samples prepared with different DipI contents.

Fresh	*Jsc* ($mA \cdot cm^{-2}$)	*Voc* (V)	*FF* (%)	*PCE* (%)
n=5	21.05 ± 0.50	0. 405 ± 0.014	63.12 ± 0.94	5.38 ± 0.28
n=10	21.26 ± 0.68	0. 411 ± 0.017	65.43 ± 2.01	5.72 ± 0.29
n=30	21.01 ± 0.67	0. 415 ± 0.011	62.31 ± 2.18	5.43 ± 0.33
n=50	21.53 ± 0.90	0. 404 ± 0.024	61.77 ± 1.75	5.36 ± 0.40

Table S2. Averaged cell parameters of devices prepared with different DipI contents upon 4-hours of light exposure in ambient conditions (air, ~60% RH).

4-hours light-soaking	*Jsc* ($mA \cdot cm^{-2}$)	*Voc* (V)	*FF* (%)	*PCE* (%)	*ΔPCE*
n=5	20.57 ± 0.40	0. 384 ± 0.016	67.33 ± 2.29	5.32 ± 0.38	-1.1%
n=10	21.08 ± 0.71	0. 409 ± 0.018	69.45 ± 1.64	5.99 ± 0.35	+4.7%
n=30	19.34 ± 0.79	0. 391 ± 0.01	65.74 ± 1.41	4.97 ± 0.15	-8.5%
n=50	19.45 ± 1.08	0. 375 ± 0.022	64.74 ± 2.87	4.73 ± 0.26	-11.8%

In a similar way, we made a preliminary basic optimization of the $NaBH_4$ content and we obtained the following results reported in Table S3. It is worth mentioning that higher $NaBH_4$ contents yielded films with low uniformity that were discarded. In view of these results we decided to fix the $NaBH_4$ concentration to 0.05M for subsequent experiments.

Table S3. Averaged cell parameters of fresh devices prepared with two different $NaBH_4$ concentrations.

Fresh	*Jsc* ($mA \cdot cm^{-2}$)	*Voc* (V)	*FF* (%)	*PCE* (%)
$NaBH_4$ (0.05 M)	20.71 ± 0.97	0.339 ± 0.01	55.43 ± 9.50	3.86 ± 0.25
$NaBH_4$ (0.1 M)	20.66 ± 0.68	0.329 ± 0.01	51.78 ± 7.84	3.50 ± 0.41

Preliminary optimization of $FASnI_3$ concentration, see Table S4, which justifies the use of a concentration of 0.8 M.

Table S4. Averaged cell parameters obtained from the fresh devices prepared with two different perovskite concentrations, with additives incorporated.

Fresh	*Jsc* ($mA \cdot cm^{-2}$)	*Voc* (V)	*FF* (%)	*PCE* (%)
0.8 M	20.04 ± 0.42	0. 411 ± 0.01	63.39 ± 1.01	5.22 ± 0.19
1 M	13.05 ± 1.22	0. 346 ± 0.02	57.16 ± 3.93	2.59 ± 0.38

SUPPLEMENTAL CHARACTERIZATION DATA

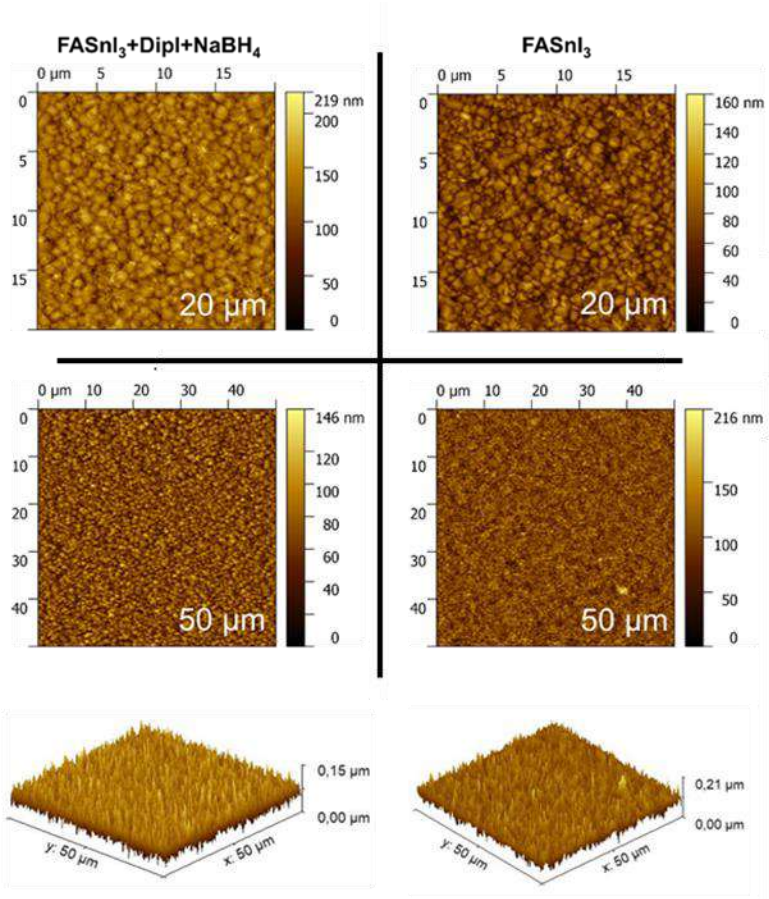

Figure S1. AFM images of $FASnI_3$+DipI+$NaBH_4$ and pristine $FASnI_3$ films. The corresponding amplitude is specified in each image.

Table S5. Roughness average (Ra) of pristine $FASnI_3$ and $FASnI_3$+DipI+$NaBH_4$ films, extracted from AFM images (figure S1).

Sample / Image size	20 microns	50 microns	Average
Pristine $FASnI_3$	3.26 nm	2.41 nm	2.83 nm
$FASnI_3$+DipI+$NaBH_4$	3.08 nm	2.08 nm	2.58 nm

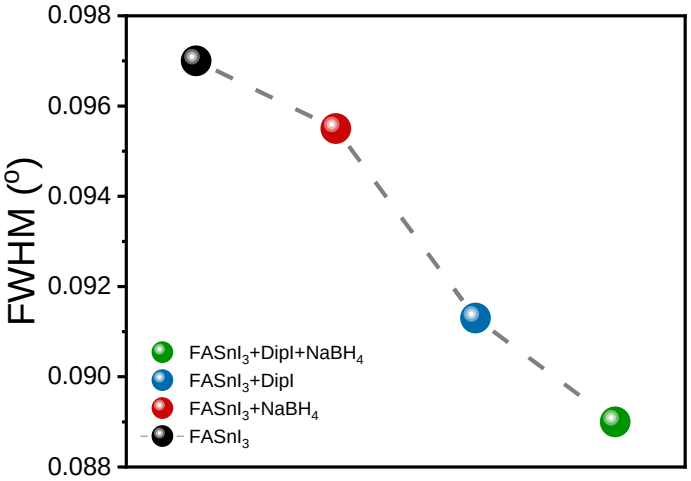

Figure S2. FWHM for the peak at 14.1°, from XRD pattern.

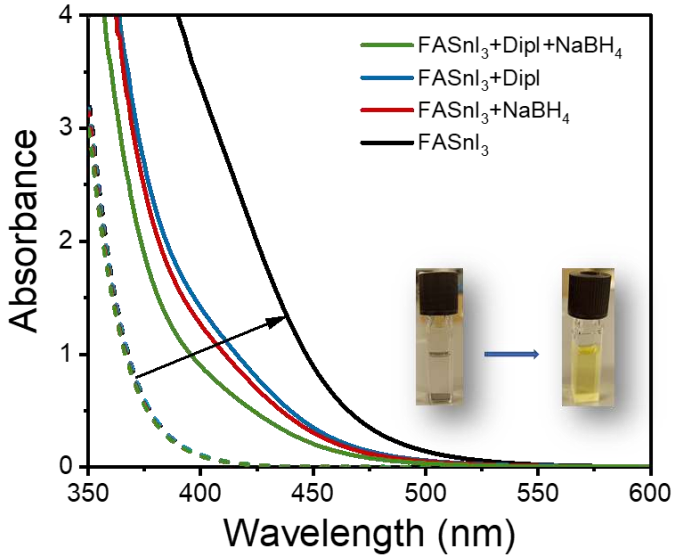

Figure S3. Absorption spectra of the Sn-HPS precursor solutions with and without the addition of additives. Dashed line indicates the absorption of fresh solutions in N_2 atmosphere, continuous line indicates the absorption of precursor solution after exposing them to air and continuous illuminated with a simulated sun AM 1.5 G for 110 minutes.

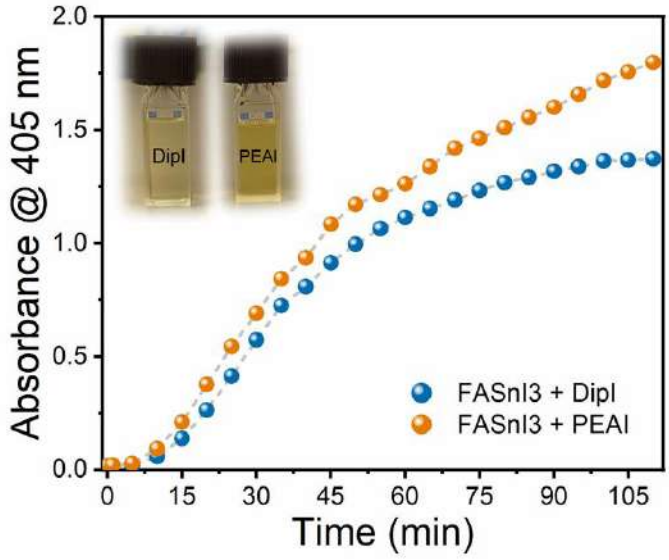

Figure S4. Absorbance evolution at 405 nm of the precursor solutions containing DipI and PEAI, respectively, upon 1 sun light-exposure in air.

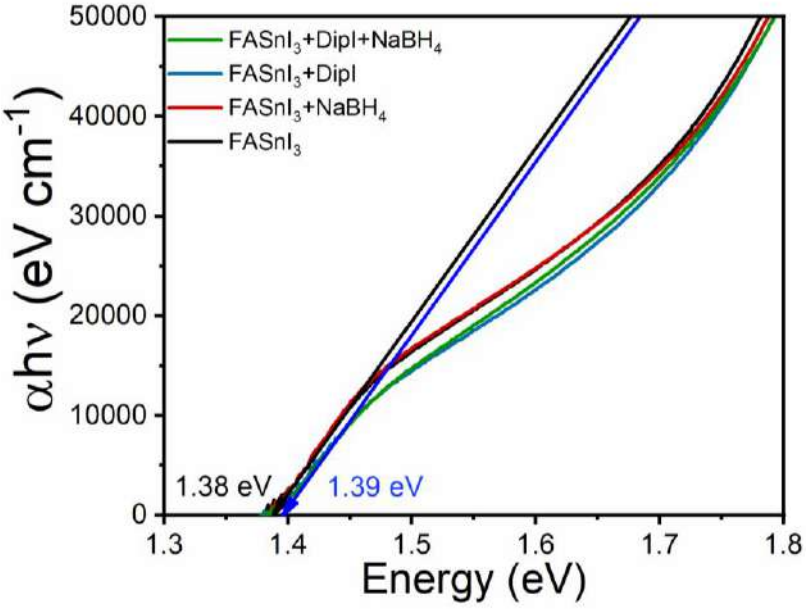

Figure S5. Tauc-plot of the $FASnI_3$ films with different additives.

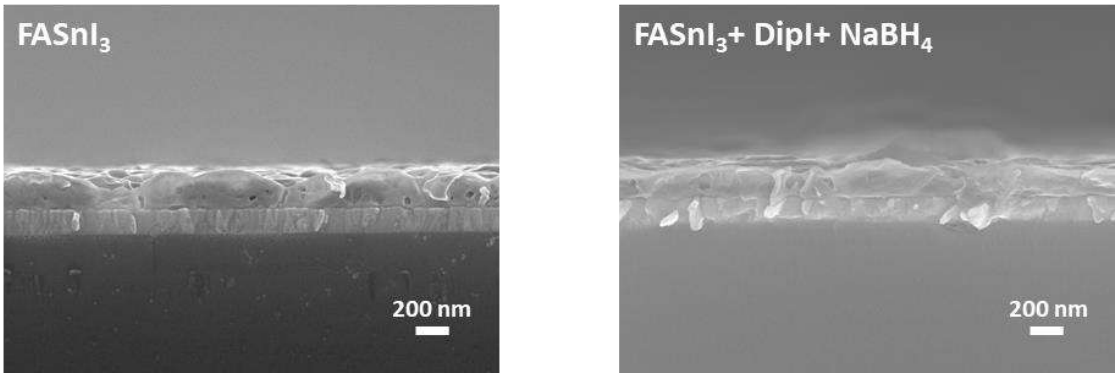

Figure S6. SEM images of the $FASnI_3$ and $FASnI_3$+DipI+$NaBH_4$ films on ITO substrates. The average thickness values were estimated to be 197 ± 40 nm and 191 ± 19 nm for $FASnI_3$ and $FASnI_3$+DipI+$NaBH_4$, respectively.

Table S6. Averaged cell parameters with the standard deviation (*Sd*) for the devices prepared with different additives after a 3-days light-soaking treatment (80 replicas for each composition).

Device	***Jsc*** ($mA \cdot cm^{-2}$)	***Voc*** (V)	***FF*** (%)	***PCE*** (%)
$FASnI_3$+DipI+$NaBH_4$	21.8 ± 0.9	0.62 ± 0.03	71 ± 3	9.6 ± 0.6
$FASnI_3$+DipI	22.6 ± 1.0	0.53 ± 0.03	69 ± 3	8.3 ± 0.4
$FASnI_3$+$NaBH_4$	21.8 ± 0.5	0.46 ± 0.01	72 ± 1	7.3 ± 0.3
$FASnI_3$	18.2 ± 1.6	0.54 ± 0.04	47 ± 6	4.8 ± 0.7

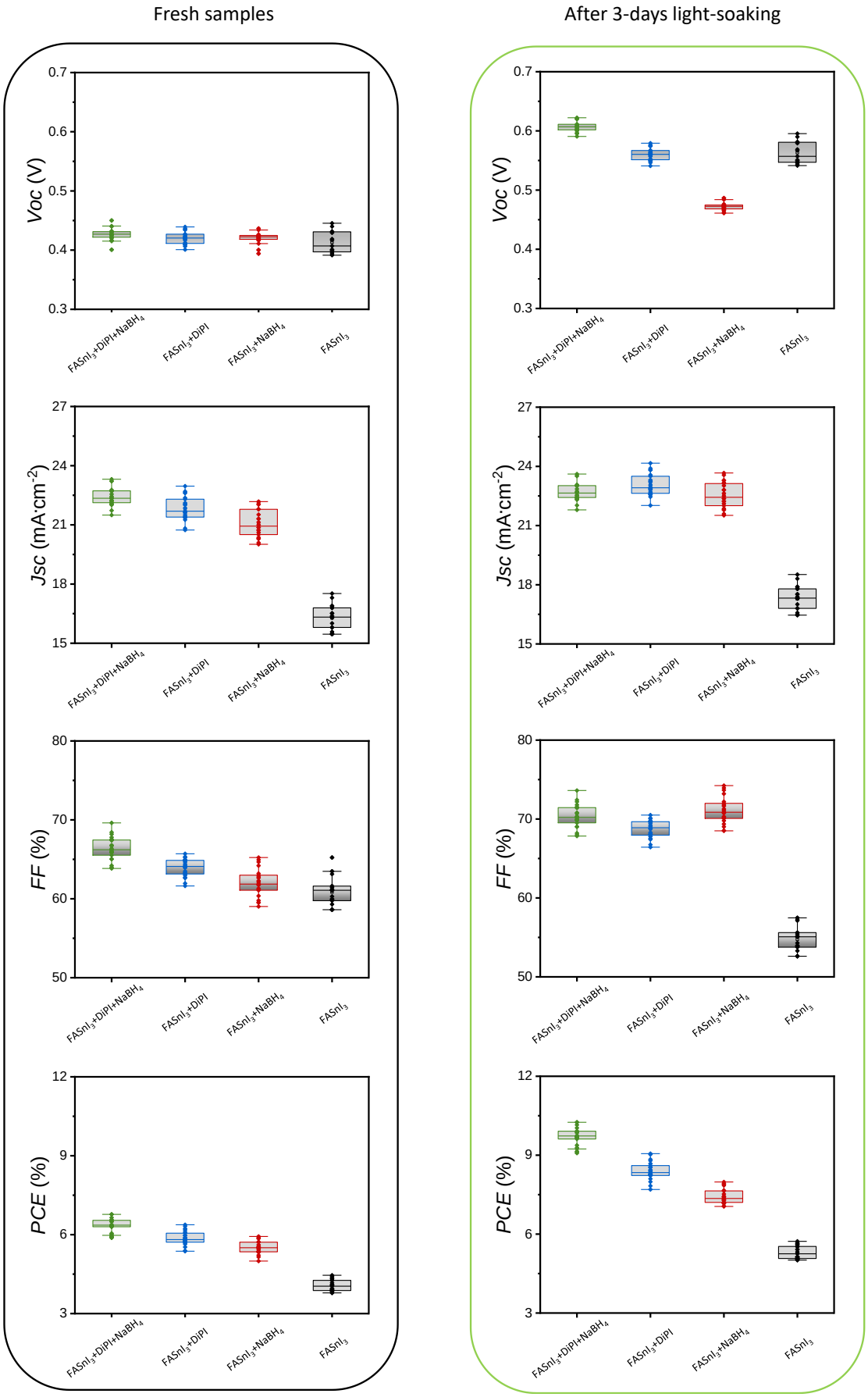

Figure S7. Statistical characterization of photovoltaic parameters of the fresh and aged devices upon 3-days under continuous illumination in inert atmosphere, respectively; all these cells were prepared in a single batch for a fairer comparison (20 replicas for each composition).

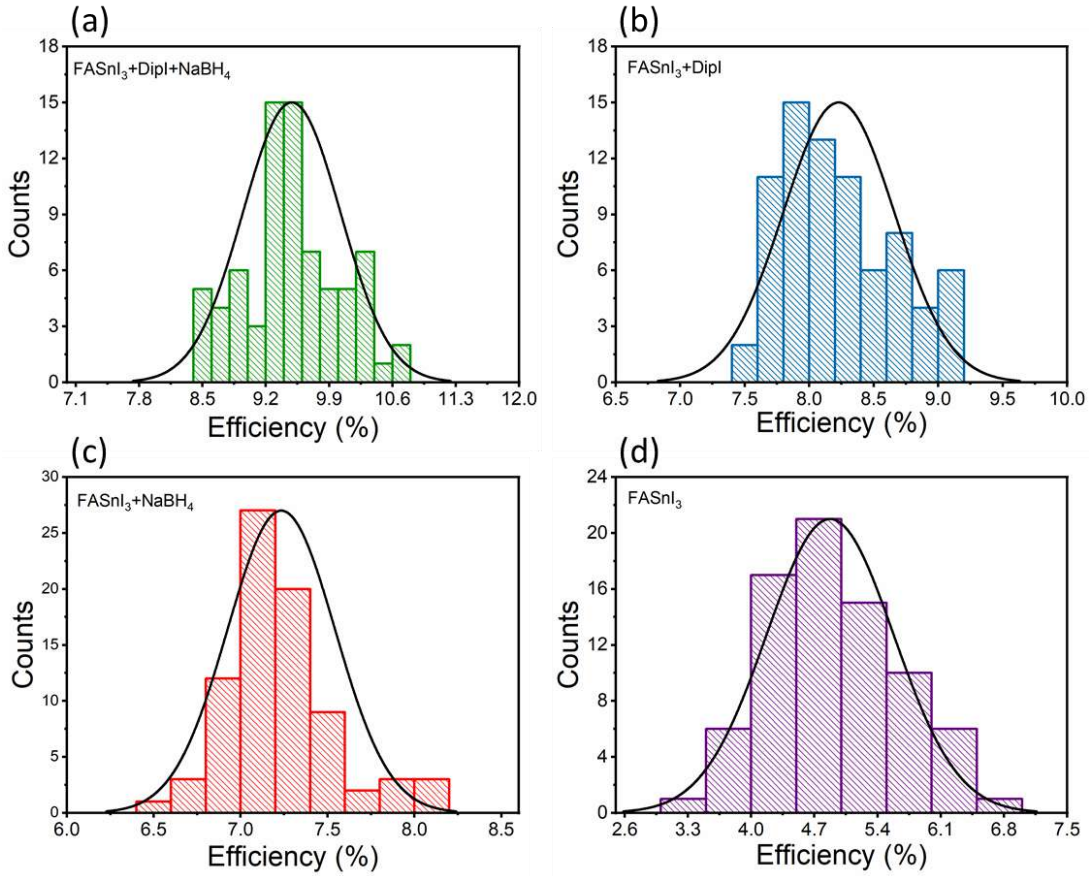

Figure S8. Efficiency histogram of 80 pixels with different additives after the 3-days light-soaking treatment. (a) $FASnI_3$+DipI+$NaBH_4$, (b) $FASnI_3$+DipI, (c) $FASnI_3$+$NaBH_4$ and (d) $FASnI_3$.

Table S7. Forward (F) and Reverse (R) parameters of $FASnI_3$ champion devices with different additive compositions after the 3-days light-soaking treatment.

Device	*Jsc* (mA·cm^{-2})	*Voc* (V)	*FF* (%)	*PCE* (%)
$FASnI_3$+$NaBH_4$+DipI-**F**	22.13	0.656	73.11	10.61
$FASnI_3$+$NaBH_4$+DipI-**R**	22.06	0.655	69.57	10.05
$FASnI_3$+DipI-**F**	23.35	0.594	65.31	9.06
$FASnI_3$+DipI-**R**	23.21	0.594	65.6	9.05
$FASnI_3$+$NaBH_4$-**F**	22.28	0.488	74.04	8.06
$FASnI_3$+$NaBH_4$-**R**	22.71	0.488	72.44	8.04
$FASnI_3$-**F**	15.82	0.642	61.04	6.20
$FASnI_3$-**R**	15.75	0.620	54.57	5.33

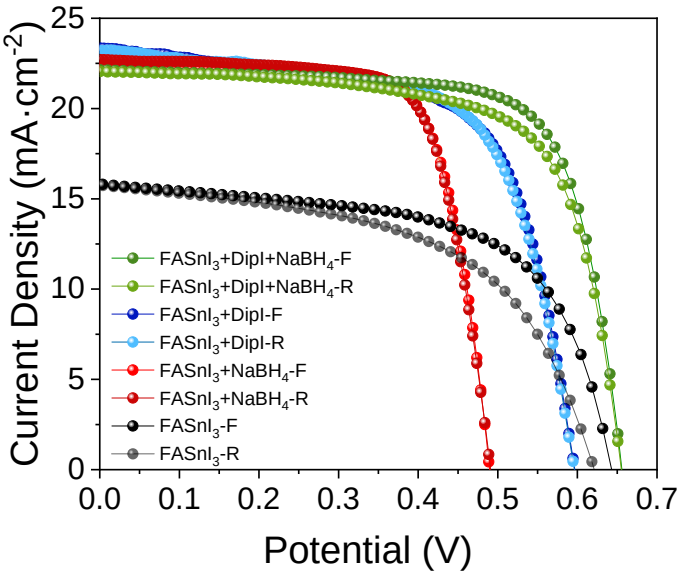

Figure S9. Forward (F) and Reverse (R) scan *J-V* curves of $FASnI_3$ champion devices with different additive compositions after the 3-days light-soaking treatment.

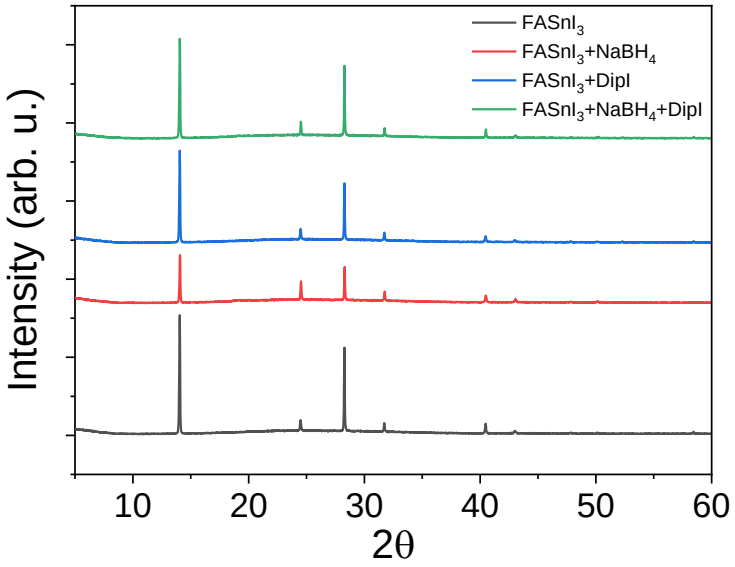

Figure S10. XRD patterns of the $FASnI_3$, $FASnI_3$+$NaBH_4$, $FASnI_3$+DipI and $FASnI_3$+DipI+$NaBH_4$ films upon 3 months stored in inert atmosphere (N_2) in the dark. The Sn-HPS diffraction peaks are unambiguously detected regardless the additive compositions after 3 months.

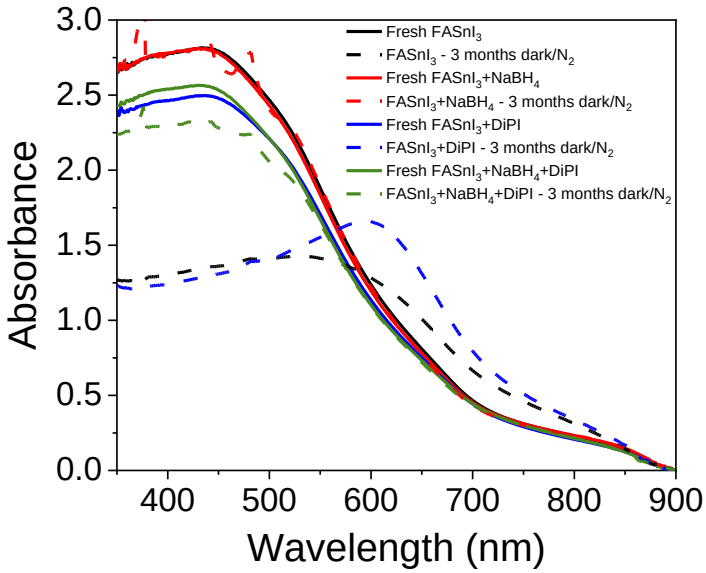

Figure S11. Comparison between the UV-Vis absorption spectra of the freshly made films and after storing them for 3 months in the dark in nitrogen atmosphere, obtained from the four studied compositions. On the one hand, the $FASnI_3$ and $FASnI_3$+DipI films suffered a dramatic change in the absorption spectra shapes and intensities; note that the absorption onset at longer wavelengths (~900 nm) and the XRD patterns showed in Figure S10 indicate that despites the clear degradation, the samples still contain the Sn-HPS phase. On the other hand, those films that contain $NaBH_4$ clearly retained the initial light absorption characteristics upon the long storage. These results allow us to partially deconvolute the effect of both additives, and indicate that $NaBH_4$ plays a direct role in the stabilization of the semiconductor when is stored in inert atmosphere.

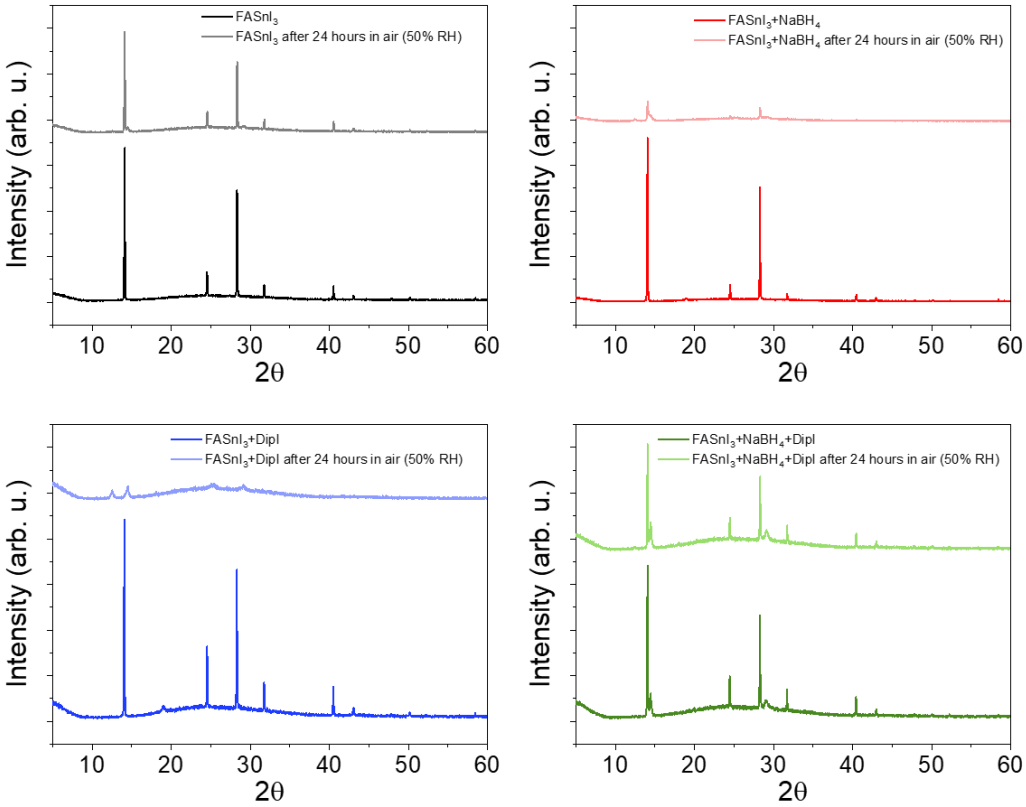

Figure S12. XRD patterns of the freshly made $FASnI_3$, $FASnI_3$+$NaBH_4$, $FASnI_3$+DipI and $FASnI_3$+DipI+$NaBH_4$ films compared to those obtained after exposing the same films to ambient atmosphere (air, ~20 ºC, ~50% R.H.) in the dark. As it can be observed, in ambient atmosphere those samples with additives degrade at similar rates or even faster, when a single additive is used, than the pristine $FASnI_3$. We hypothesize that due to the high hygroscopic nature of both, $NaBH_4$ and DipI, the ambient moisture can be more efficiently fixed in

the Sn-HPS and subsequent degradation reactions are created and/or accelerated. In fact, it is well known that $NaBH_4$ reacts with water molecules according to the following reaction (eq. 1):

$$NaBH_4 + 2H_2O \rightarrow NaBO_2 + 4H_{2\,(g)} \qquad (1)$$

Note that equation 1 is the simplified version of a complex mechanism that involve intermediates and products that may accelerate the Sn-HPS degradation; in fact, this reaction is catalyzed by metals if water is present.[1] Therefore, the complexity of the chemistry involved in the degradation mechanisms of Sn-HPS and the great number of variables that seem to play a role, *i.e.* additives, tin oxidation, halides chemistry, atmosphere, illumination, moisture, etc., further investigation is required for a deeper understanding of the exact mechanisms that our additives play on the stability of the Sn-HPS films.

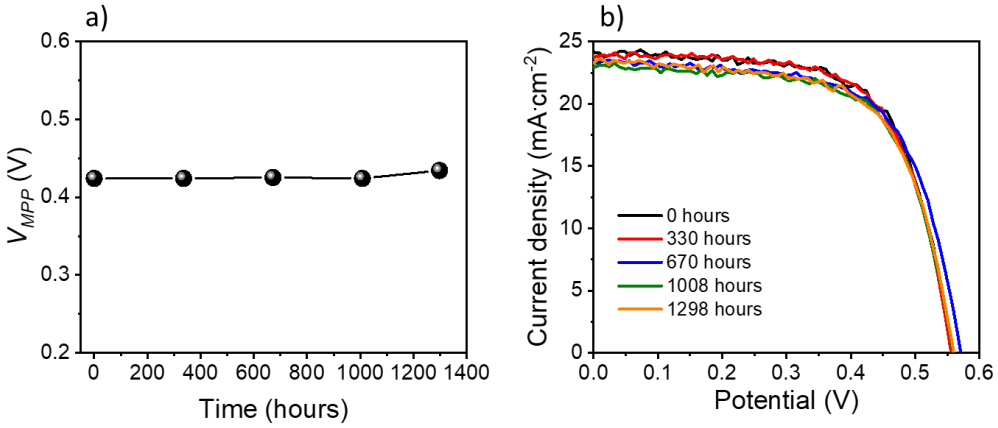

Figure S13. Electrical characterization of a $FASnI_3$+DipI+$NaBH_4$ device at *MPP*: a) V_{MPP} evolution and b) *J-V* curves measured throughout the *MPP* experiment. V_{MPP} are directly extracted from the *J-V*s. It is important to highlight that *MPP* stability measurements where not performed using a *MPP* tracker but at fixed voltage, and consequently strictly speaking our experiment could be considered a *quasi-MPP* experiment. However, as it is clearly observed, the V_{MPP} remains almost invariable along the experiment, which demonstrates that our measuring conditions are very close to the real *MPP*, so we use this terminology.

Table S8. V_{MPP} values at different intervals extracted from the above *J-V* curves.

	0 hours	330 hours	670 hours	1008 hours	1298 hours
V_{MPP}	0.424	0.424	0.425	0.424	0.434

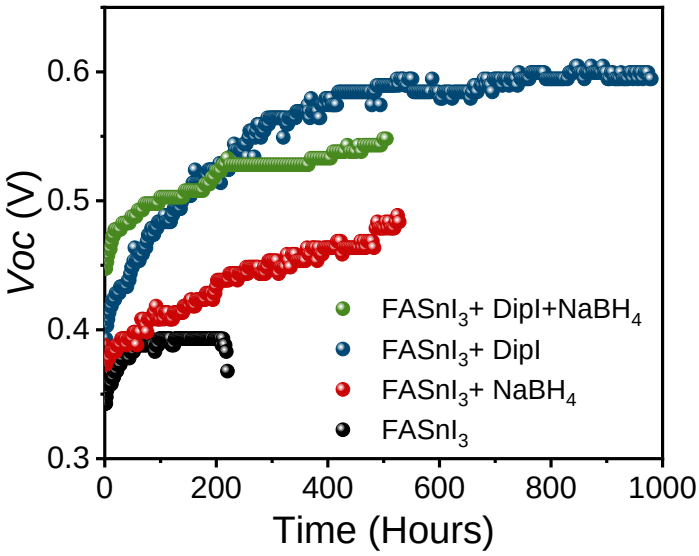

Figure S14. Comparison of the *Voc* evolution among the pristine $FASnI_3$, $FASnI_3$+DipI, $FASnI_3$+$NaBH_4$ and $FASnI_3$+DipI+$NaBH_4$ devices under continuous illumination in N_2 atmosphere. Data obtained from *J-V* curves registered every two hours. The illumination was carried out using a UV cut-off filter; which was only used in the experiments shown in Figures 5b, S11 and S12, not for the rest of the experiments in the manuscript.

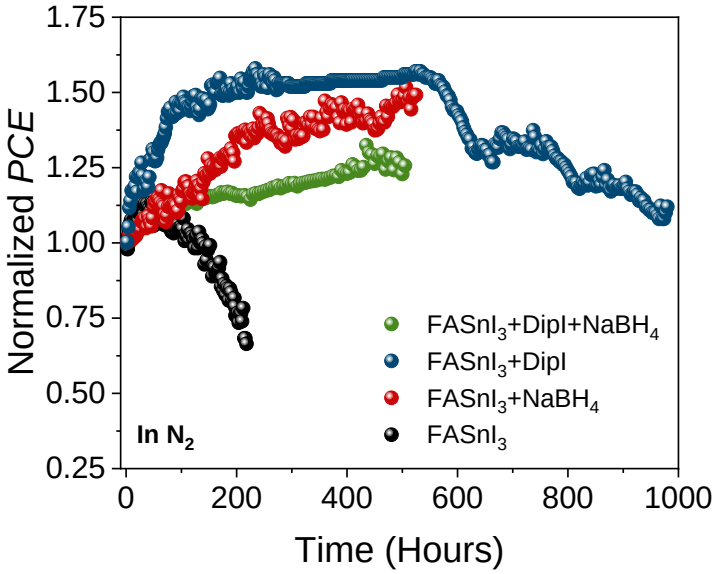

Figure S15. Normalized efficiency of devices without and with different additives, after exposing them to continuous illumination in N_2 atmosphere. The *J-V* curves were registered every 2 hours. Illumination was with a UV-cut-off filter. This filter was only used in the experiments shown in Figures 5b, S11 and S12, not for the rest of the experiments in the manuscript.

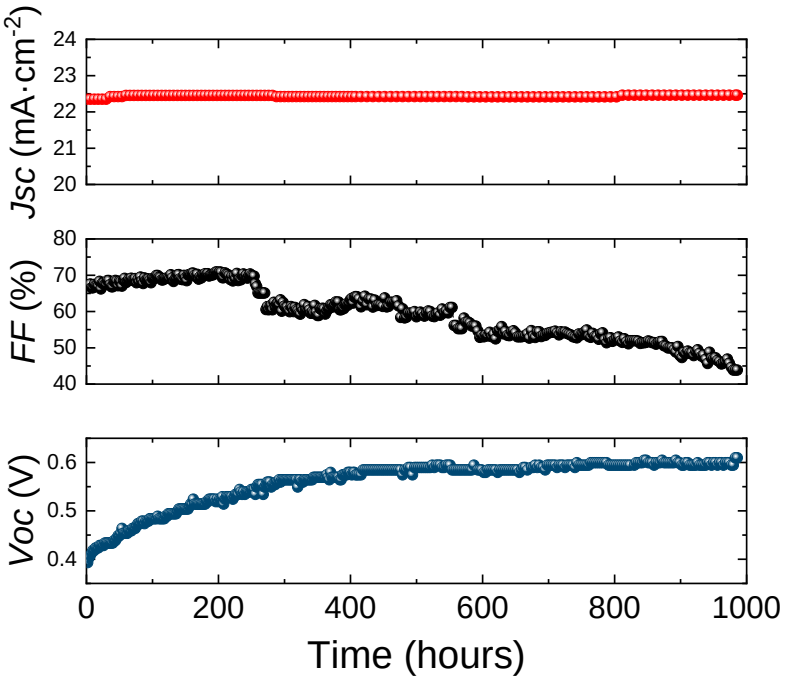

Figure S16. *Jsc*, *FF* and *Voc* behavior of the $FASnI_3$+DipI device after 1000 hours of continuous illumination in N_2 atmosphere.

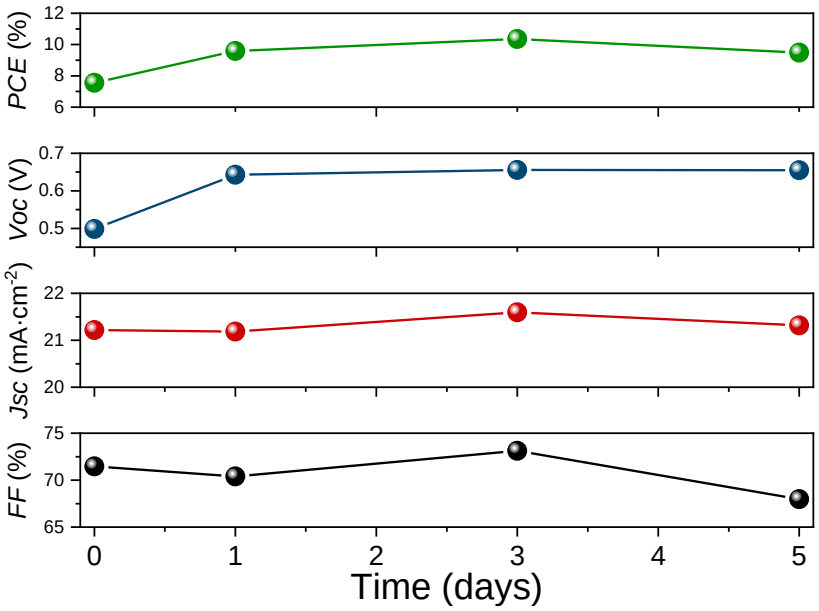

Figure S17. Cell parameters of a $FASnI_3$+DipI+$NaBH_4$ device after several days of light-treatment with a solar simulator (AM1.5G) in N_2 atmosphere.

Table S9. Summary of stability of Sn-HPS with different additives.

PS composition	Stability conditions	Time	*PCE* retained	Additives	Year
$CsSnI_3$	Shelf stability in N_2	250 hours	100 %	SnF_2	2014[2]
$CsSnI_3$	Shelf stability in N_2	10 days	90 %	SnI_2	2015[3]
$CsSnI_3$	Unencapsulated at continuous 1 sun irradiation in 25% RH	16 hours	70 %	$SnCl_2$	2016[4]
$CsSnBr_3$	Unencapsulated, shelf stability in 40% RH	5 hours	40 %	SnF_2 and hydrazine	2017[5]
$CsSnI_3$	Unencapsulated, continuous 1sun irradiation in 40% RH	30 min	40 %	$SnCl_2$ and piperazine	2018[6]
$FASnI_3$	Encapsulated at *MPP* in 50% RH	100 hours	100 %	SnF_2 and 5-AVAI	2018[7]
$FASnI_3$	Unencapsulated, continuous 1 sun irradiation in 20% RH	16 hours	50 %	$SnCl_2$ and KHQSA	2018[8]
$FASnI_3$	Continuous 1 sun irradiation in N_2	350 hours	60 %	SnF_2 and TFEACl	2019[9]
$FASnI_3$	Encapsulated at *MPP* in 20% RH	600 hours	93 %	SnF_2 and FBH	2020[10]
$Cs_{0.2}FA_{0.8}SnI_3$	Encapsulated at *MPP* in N_2	1000 hours	95 %	SnF_2 and $SnCl_2$	2020[11]
$FASnI_3$	Encapsulated at *MPP* in N_2	1000 hours	95 %	SnF_2 and PAI	2020[12]
$FA_{0.75}MA_{0.25}SnI_3$	Shelf stability in N_2	1000 hours	92 %	SnF_2 and FACl	2022[13]
$FASnI_3$	Unencapsulated at *MPP* in 60% RH	9 hours	80 %	SnF_2, DipI and $NaBH_4$	2022*****
$FASnI_3$	Unencapsulated at *MPP* in N_2	1300 hours	96 %	SnF_2, DipI and $NaBH_4$	2022*****

*****This work

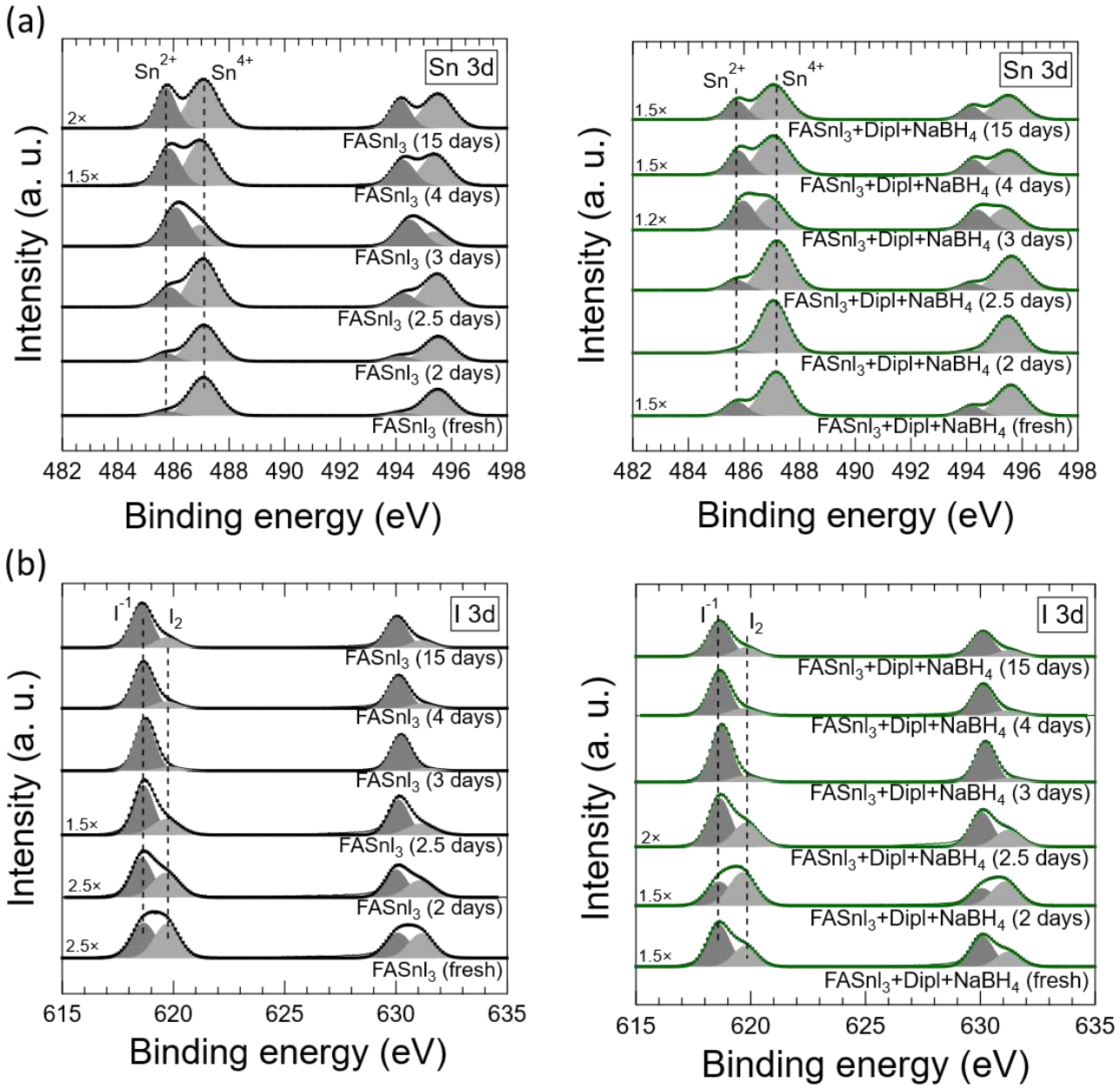

Figure S18. Evolution of the composition of the $FASnI_3$ and $FASnI_3$+DipI+$NaBH_4$ films, respectively, at different illumination times; (X days) indicated for each sample, where X is the light-soaking time at 1 sun in N_2 atmosphere: (a) Sn^{+2}/Sn^{+4} and (b) I^-/I_2 ratios.

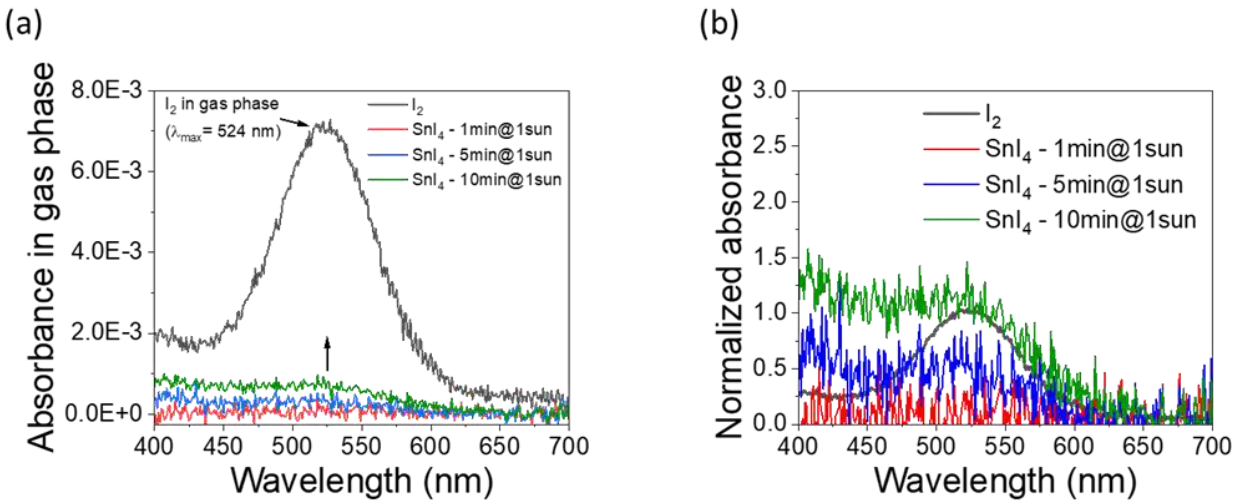

Figure S19. UV-Vis characterization: (a) Absorption spectra of I_2 in gas phase (black line) and monitorization of the I_2 formation upon illumination (1 sun) of SnI_4 powder at room temperature in inert atmosphere. For the control measurement, a small I_2 crystal was introduced in a spectroscopy quartz cuvette and the spontaneous sublimation of I_2 allowed measuring its absorption spectrum in gas phase. For monitoring the photoinduced formation of I_2, a small amount of SnI_4 powder was introduced in a quartz cuvette, purged with a continuous argon flow during 2 minutes and subsequently illuminated/measured at different intervals; a prominent signal that perfectly matches with the I_2 absorption is gradually identified. (b) Normalized absorption spectra of the reference gas phase I_2 and the photogenerated I_2 upon exposing 1, 5 and 10 minutes, respectively, the SnI_4 powder to light. The 10 minutes curve was normalized to unity at λ=524 nm, and for the 1- and 5-minutes curves the same normalization factor was applied.

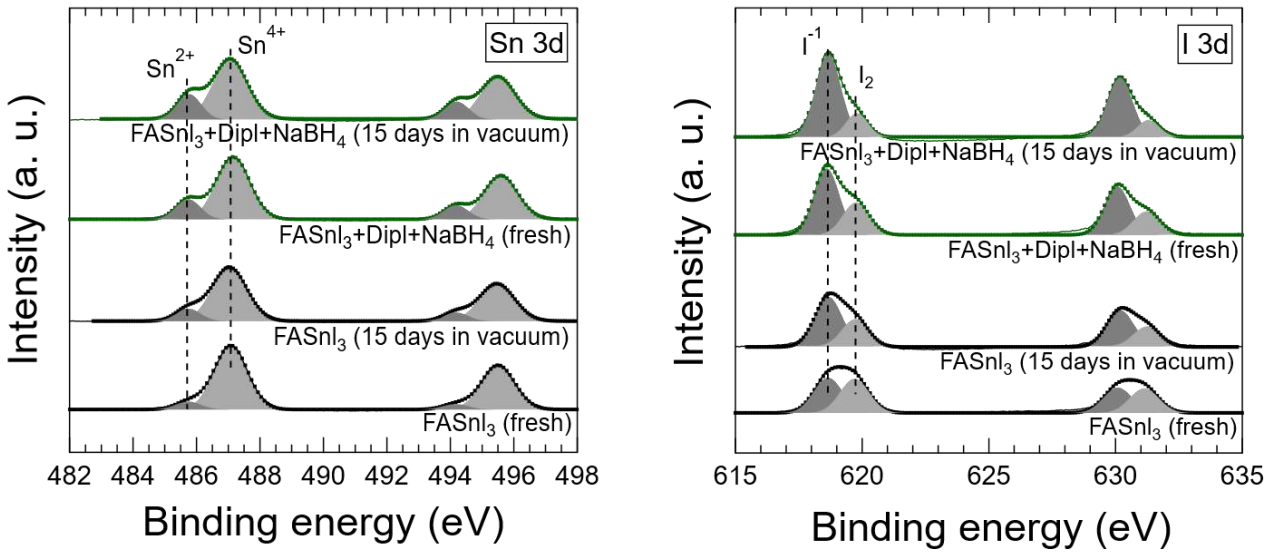

Figure S20. Sn^{+2}/Sn^{+4} and I^-/I_2 ratios of the $FASnI_3$ and $FASnI_3$+DipI+$NaBH_4$ films, respectively, after being stored 1 and 15 days in the XPS sample compartment in ultra-high vacuum conditions. (X days) indicated for each sample, where X is the light-soaking time at 1 sun in N_2 atmosphere.

SUPPLEMENTAL REFERENCES

1. Abdelhamid, H.N. (2021). A review on hydrogen generation from the hydrolysis of sodium borohydride. Int. J. Hydrog. Energy *46*, 726-765. https://doi.org/10.1016/j.ijhydene.2020.09.186.

2. Kumar, M.H., Dharani, S., Leong, W.L., Boix, P.P., Prabhakar, R.R., Baikie, T., Shi, C., Ding, H., Ramesh, R., and Asta, M.J.A.M. (2014). Lead-free halide perovskite solar cells with high photocurrents realized through vacancy modulation. Adv. Mater**.** *26*, 7122-7127. https://doi.org/10.1002/adma.201401991.

3. Marshall, K.P., Walton, R.I., and Hatton, R.A. (2015). Tin perovskite/fullerene planar layer photovoltaics: improving the efficiency and stability of lead-free devices. J. Mater. Chem. A *3*, 11631-11640. https://doi.org/10.1039/C5TA02950C.

4. Marshall, K.P., Walker, M., Walton, R.I., and Hatton, R.A. (2016). Enhanced stability and efficiency in hole-transport-layer-free CsSnI3 perovskite photovoltaics. Nat. Energy *1(12)*, 1-9. https://doi.org/10.1038/nenergy.2016.178.

5. Song, T.-B., Yokoyama, T., Stoumpos, C.C., Logsdon, J., Cao, D.H., Wasielewski, M.R., Aramaki, S., and Kanatzidis, M.G. (2017). Importance of Reducing Vapor Atmosphere in the Fabrication of Tin-Based Perovskite Solar Cells. J. Am. Chem. Soc. *139*, 836-842. https://doi.org/10.1021/jacs.6b10734.

6. Song, T.-B., Yokoyama, T., Logsdon, J., Wasielewski, M.R., Aramaki, S., and Kanatzidis, M.G. (2018). Piperazine Suppresses Self-Doping in CsSnI3 Perovskite Solar Cells. ACS Appl. Energ. Mater. *1*, 4221-4226. https://doi.org/10.1021/acsaem.8b00866.

7. Kayesh, M.E., Matsuishi, K., Kaneko, R., Kazaoui, S., Lee, J.-J., Noda, T., and Islam, A. (2019). Coadditive Engineering with 5-Ammonium Valeric Acid Iodide for Efficient and Stable Sn Perovskite Solar Cells. ACS Energy Letters *4*, 278-284. https://doi.org/10.1021/acsenergylett.8b02216.

8. Tai, Q., Guo, X., Tang, G., You, P., Ng, T.-W., Shen, D., Cao, J., Liu, C.-K., Wang, N., Zhu, Y., et al. (2019). Antioxidant Grain Passivation for Air-Stable Tin-Based Perovskite Solar Cells. Angew. Chem. Int. Ed. *58*, 806-810. https://doi.org/10.1002/anie.201811539.

9. Yu, B.-B., Xu, L., Liao, M., Wu, Y., Liu, F., He, Z., Ding, J., Chen, W., Tu, B., Lin, Y., et al. (2019). Synergy Effect of Both 2,2,2-Trifluoroethylamine Hydrochloride and SnF2 for Highly Stable FASnI3−xClx Perovskite Solar Cells. Sol. RLL *3*, 1800290. https://doi.org/10.1002/solr.201800290.

10. He, X., Wu, T., Liu, X., Wang, Y., Meng, X., Wu, J., Noda, T., Yang, X., Moritomo, Y., Segawa, H., and Han, L. (2020). Highly efficient tin perovskite solar cells achieved in a wide oxygen concentration range. J. Mater. Chem. A *8*, 2760-2768. https://doi.org/10.1039/C9TA13159K.

11. Liu, X., Wang, Y., Wu, T., He, X., Meng, X., Barbaud, J., Chen, H., Segawa, H., Yang, X., and Han, L. (2020). Efficient and stable tin perovskite solar cells enabled by amorphous-polycrystalline structure. Nat. Commun. *11*, 2678. https://doi.org/10.1038/s41467-020-16561-6.

12. Liu, X., Wu, T., Chen, J.-Y., Meng, X., He, X., Noda, T., Chen, H., Yang, X., Segawa, H., Wang, Y., and Han, L. (2020). Templated growth of FASnI3 crystals for efficient tin perovskite solar cells. Energy Environ. Sci. 13, 2896-2902. https://doi.org/10.1039/D0EE01845G.

13. Zhou, J., Hao, M., Zhang, Y., Ma, X., Dong, J., Lu, F., Wang, J., Wang, N. and Zhou, Y. (2022). Chemo-thermal surface dedoping for high-performance tin perovskite solar cells. Matter *5*, 683-693. https://doi.org/10.1016/j.matt.2021.12.013.